MSc thesis in Materials Science and Engineering

Finite element modelling of viscoelastic spinoidoid metamaterials

Julia Czarnecka

August 2023

A thesis submitted to the Delft University of Technology in partial fulfilment of the requirements for the degree of Master of Science in Materials Science and Engineering

Abstract

Recent advancements in additive manufacturing have led to significant progress in the field of metamaterials, wherein the introduction of microscopic features affects the material properties on a macroscale. Common examples of these materials are truss-based and plate-based structures. However, these lattices bear inherent susceptibility to stress concentration points, which undermine their overall performance. Incorporating smooth surfaces in the material design can be a promising strategy for solving that issue. One noteworthy class of smooth metamaterials originates from the topologies formed in the process of spinodal decomposition. For small fluctuations, these structures can be described mathematically using Gaussian random fields (GRF) stemming from the superposition of standing waves. Recent research work has led to the development of a subtype of these structures, termed spinodoids. Spinodoids are anisotropic structures formed through a biased sampling of wave direction vectors encompassing the underlying GRF.

The development of spinodoid topologies has allowed for extensive design exploration and property-structure investigations, important in the context of many potential future applications, such as bone biomaterials design. Until now, the majority of studies performed on spinodoid metamaterials were limited to the elastic regime. However, many materials, especially biological tissues such as bone, rarely exhibit purely elastic behaviour. Thus, exploring other material regimes is of great interest. This work attempts a finite element analysis of three different types of spinodoid structures: lamellar, cubic, and columnar. These structures' properties are based on a generalized Maxwell model for cortical bone. The study explores how tuning the design parameters influences their mechanical behaviour in a viscoelastic regime.

Contents

List of Figures

1 Introduction

Bone is a vital tissue with many functions in the human body. It provides mechanical support for the soft tissues, it is the main location of blood cell formation, and it contributes to maintaining mineral homeostasis [1]. Bone tissue is dynamic in nature, which means that it is continuously remodelling itself to maintain skeletal integrity, and is therefore capable of self-repairing. However, in many cases of serious trauma, which is of higher risk with increasing age, surgical intervention becomes necessary to facilitate bone regeneration. It is hence no surprise that in the era of the ageing population, bone is the second most often transplanted tissue [1]. While autogenous bone grafts, i.e., grafts taken from the patient's own bone, are still the most desired due to their superior osteogenic properties [2], limited material availability often makes autotransplantation impossible. Allografts, which are bone grafts obtained from other human donors, have also been clinically implemented. Although there are virtually no material quantity limitations with these types of grafts, the concerns about disease transmission and immune responses are still in place [3].

These issues have urged scientists to look for alternative solutions in bone defect treatment, such as using artificial bone implants, conventionally made out of titanium or stainless steel. Recently, the research focus moved also towards biodegradable metals, such as magnesium or iron. Spontaneous biomaterial degradation in vivo can be very beneficial, as it removes the necessity of removal surgery upon healing, significantly reducing risks and costs for the patient. The bone tissue engineering (BTE) approach is another strategy focusing on the temporary fixation of the supporting substrate to facilitate tissue regeneration. It combines the usage of biodegradable scaffolds together with signalling factors to promote cellular response, angiogenesis (new blood vessel formation), and bone tissue regeneration [1]. Naturally, there is a range of requirements that need to be fulfilled for an implant or scaffold to effectively serve its purpose, such as ensuring that it has adequate mechanical properties, matching those of the surrounding bone tissue [4]. Careful tuning of parameters such as stiffness is essential to provide sufficient mechanical support for tissue regeneration, while also minimising the risk of stress shielding and, consequently, bone atrophy. An additional difficulty in the scaffold design is linked to the large variability of bone tissue's mechanical characteristics not only within a single bone but also between individual patients. As a result, the optimal design of a bone scaffold, which can be easily tunable to the needs of the patient, remains a challenge.

In recent years, numerous studies have been carried out on scaffolds based on *mechanical metamaterials*, i.e. materials whose mechanical behaviour in macroscale is a result of their architectured features on an intermediate level[5]. The ability to tune the structure of the material down to the microscale, and through that control its properties on the macroscale, opens up new possibilities in the implant and scaffold design space. Many researchers hope that through the developments in the metamaterial field, we will get closer to finding a reliable bone graft substitute, and eventually make the bone regeneration treatment more effective, more widely accessible and more affordable. [6]

Thus far, the majority of tests on the mechanical behaviour of the spinodal focused on the elastic behaviour of those structures only, while bone tissue itself exhibits a more complex mechanical response. The aim of this work is to extend the testing of the spinodoid

topologies to include also matching the design parameters in the viscoelastic regime.
The described problem is an example of an application for spinodoid structures, which served as a starting point and inspiration for the literature review preceding the thesis project. Hence, this problem will be elaborated upon further, with the aim for it to serve as an example of the context in which this study can be considered. However, it is important to note that the described example serves as a starting point in a broader narrative, and the general premise of this work is to explore the mechanical response of various spinodoid structures overall, not necessarily in the context of their application in the bone biomaterial field.

2 Literature review

2.1 Point of departure - biomaterials for bone regeneration

In order to design a fitting bone implant or scaffold, the anatomy and specific nature of bone tissue need to be understood. The key macroscale structural elements to distinguish are the trabecular bone (also called spongy bone), the cortical (compact) bone, and the medullary cavity, in which the bone marrow resides [7]. It has to be noted that each of these anatomical units has diametrically different mechanical properties. For example, it can be easily deduced that cortical bone has on average higher stiffness than spongy bone - the elastic modulus of the spongy bone can be as low as 0.02 GPa, in comparison with 30 GPA for cortical bone.[8] Bone marrow, in turn, is a semi-solid, soft tissue, which can be studied in terms of its elastic, viscoelastic as well as fluid constitutive properties. The microstructural composition of the bone can be divided into the matrix and the cellular component. There are three main types of distinctly specialised cells present in the bone tissue, namely osteoblasts, osteoclasts, and osteocytes. Osteoblasts produce the extracellular matrix (consisting primarily of collagen) and are hence responsible for bone growth and bone deposition. The function of osteoclasts is to aid with bone resorption. Both bone deposition and bone resorption are parts of the continuous process of bone remodelling, which is guided by the osteocytes. Osteocytes, which constitute over 95% of all the cells in the bone tissue, are responsible for mechanosensing and regulating the activity of osteoclasts and osteoblasts. The remaining component of the bone, i.e., the matrix, can be divided into the organic and the inorganic constituents. The inorganic constituent comprises crystals of calcium- and phosphate-based mineral, i.e. *hydroxyapatite* (chemical formula: $Ca_{10}(PO_4)_6(OH)_2$), which amounts to over 65 % of the bone mass. The organic part of the bone matrix is mainly built up of collagens and includes also other non-collagenous proteins and mucopolysaccharides.

An important feature of the bone tissue is its hierarchical structure across multiple length scales, which ultimately gives rise to the bone's unique mechanical behaviour on the macroscale. Both the cortical and the trabecular bone are built up from fibres, which are comprised of smaller fibrils and microfibrils. On an even smaller scale, the basic building block of collagen microfibrils, *tropocollagen*, is a 300 nm long triple helix, made out of three intertwined polypeptide chains. The tropocollagen units form intricate arrangements with hydroxyapatite nanocrystals, which effectively give rise to bone's macroscopic fracture toughness. A scheme of bone tissue architecture was presented in Figure **??**, and the relevant length scales for different structural elements were indicated.

This work will not discuss the details regarding each individual level of the hierarchal arrangement in the bone tissue due to the length constraints. It aims only to recognize the link between the bone's intrinsic multiscale structure and the resulting mechanical properties, and hence to highlight the importance of incorporating micro- and nanoscale features in the design of bone regeneration biomaterials.

The design of biomaterials for bone regeneration is, intrinsically, a multi-objective problem. In order to ensure the full safety and functionality of any implant, or scaffold, which is to

be put into use *in vivo*, many parameters and metrics need to be considered. Before delving into the details of these requirements, the terminology used throughout this work shall be briefly clarified. The term *biomaterial* is applied here to generally refer to a "non-viable material used in a medical device intended to interact with biological systems"; which thus includes both bone implants and bone scaffolds.[9] The main distinction between an implant and a scaffold is that implants are usually intended to be permanent fixations, while scaffolds are thought of as temporary platforms. Nevertheless, since in the literature the distinction between the two can often be more blurry, i.e. biodegradable magnesium biomaterials may be referred to as implants, and since the key design criteria elaborated upon in this work are applicable to both bone implants and scaffolds, the two will not be treated separately in the general analysis.
Arguably the most important feature of any biomaterial is its biocompatibility with the host tissue. For a bone tissue engineering scaffold, this additionally means that the introduced cellular support substrate will not only have to remain bioinert but also that it will facilitate the molecular and mechanical signalling to aid with tissue regeneration, while at the same time, it will not cause any adverse local or systemic reactions in the host tissue.[10] Additionally, as by default, the scaffold is intended to be fully biodegradable, its degradation rate and any degradation byproducts need to be carefully controlled to ensure safe and successful treatment. Overall, three consecutive phases can be distinguished in the bone defect healing process: inflammation, repair and reconstruction. Especially during the inflammation and repair stages, where the bone on the injury site is virtually incapable of carrying any loads, it needs to be ensured that sufficient mechanical support is provided through the implant or scaffold. Otherwise, there might be secondary damage or a fracture arising on the site. During the last regeneration stage, however, in the case of a non-permanent fixation, the gradual increase of the load in the bone is necessary in order to reintroduce the load-bearing capacity of the bone.[3] Hence, the subsequent steps of the bone healing process require precise control of the biomaterial's degradation rate in time.
When designing biomaterials specifically for bone tissue regeneration, it is important to consider the *osteoconductive* and *osteoinductive* properties. Osteoconduction refers to the functionality to provide a matrix, i.e., a substrate to which the cells can attach, facilitating the invasion of blood cells and bone formation - *osteogenesis*. Osteoinduction pertains to the presence of biological mediators, for example, growth factors, that stimulate the recruitment of mesenchymal stromal cells (MSCs). Abundant in the bone marrow, MSCs are the progenitor cells capable of differentiating into osteoblasts and osteocytes among other cell types. Hence, for the most effective bone regeneration stimulation, the combination of the three elements is needed: a matrix, the bone-forming cells, as well as the inducing factors. Several BTE scaffold designs might also incorporate responsiveness to various stimuli, such as temperature, pH, or even the presence of a specific protein, with the aim of introducing more precise tailoring of the scaffold to an irregular bone defect and effectively making the surgical procedure less invasive.

2.1.1 Mechanical consideration in biomaterial design

Nevertheless, some of the most crucial scaffold and implant requirements relate to their structural and mechanical design and, consequently, the desired mechanical behaviour in vivo, which is the primary focus of this work. As predicted by Wolff's law, the placement of a biomaterial with inappropriately tuned stiffness may result in surrounding bone

resorption due to the stress shielding effect. One strategy to achieve the desired mechanical behaviour of the scaffold/implant relies on the selection of a bulk material with mechanical properties matching those of the bone tissue as closely as possible. Utilizing specific processing routes, or using methods to alter the microstructure and/or composition of the bulk material, such as alloying, allows for a constant improvement of these characteristics. For instance, the family of TNZT titanium alloys containing niobium zirconium and tantalum enables achieving stiffness in a range of 50 GPa, compared to ∼110 GPa for a conventional Ti-6Al-4V biomedical alloy. However, this approach has its limits in terms of material selection and processing, both for implants and scaffolds - as seen in the example of Ti-based implants, 50 GPa is still significantly higher than average cortical bone stiffness [11]. Not only the stiffness, but also other mechanical properties, such as the yield strength, Poisson's ratio, and the reduction of any points of internal stress concentrations for optimal fatigue life, among others, are of utmost importance. Various other parameters related to the scaffold's and implant's design and topology also have a crucial effect on the final performance of the biomaterial. The optimally designed structure should possess a sufficient porosity percentage and distribution, and it should mechanically stimulate the newly formed tissue on the biomaterial/bone interface in the pores. A sufficient level of porosity also increases the interface area between the tissue and the material and ensures appropriate fluid transport properties, which are necessary to facilitate proper nutrient supply and waste removal on the implantation site. [12] Studies have shown that optimal pore size in the implants and scaffolds should correspond to the sizes of the relevant features in the bone tissue, and hence be in a range of 400-600 microns.
A strategy to optimise both the amount of porosity, as well as to tune the material's mechanical properties without the necessity of compositional changes, involves the reduction of the relative density ($\overline{\rho}_0$). Relative density is effectively a fill fraction of the structure, i.e. the density of the structure relative to the density of the bulk material. Conversely, the amount of porosity, ϕ, also referred to as the volume fraction of the void space in the structure, can be described using the equation $\phi = 1 - \rho_0$. [12] A low relative density can be a feature of non-periodic, stochastic structures, such as metallic foams. An example of stochastic structures for bone regeneration applications is porous tantalum implants. Alternatively, porosity can be introduced by carefully designing the material's structure on the microscale, resulting in the creation of a periodic mechanical metamaterial. These specific structures will be introduced and discussed in detail in the latter part of the work.

2.2 Metamaterials

During the material selection process, one often strives to pick a material with very specific mechanical properties for the desired application. This is certainly the case, for example, when designing a biomaterial structure for bone regeneration. One conventional pathway to achieve desired mechanical properties is by introducing compositional alterations in the bulk material, which is often very challenging.
Recent advances in the field of 3D printing enable an approach alternative to using bulk materials, which focuses on *metamaterials* (also referred to as architected or cellular materials). Contrary to conventional materials, which are influenced primarily by their intrinsic constituents, the mechanical properties of mechanical metamaterials stem from their periodic or stochastic structural architecture on a microscale. [13] With regards to biomaterial applications specifically, the term *meta-biomaterials* might also be encountered in

the literature. It has been coined to describe materials with microstructural features designed to achieve specific mechanical, biological or mass-transport properties.[14] An introduction of an intermediate-level architecture opens up new possibilities for biomaterial design in terms of many (multi)functionalities. The primary focus of this work onward will be on how the intermediate structure influences the material's mechanical behaviour; nonetheless, it is important to keep in mind that it can simultaneously impact other material characteristics as well, and which might be important for the desired application of the metamaterial. This can be explained, using the example of metamaterials used for bone biomaterials – it has been shown that certain metamaterials can promote cellular adhesion more effectively, compared to the same bulk material. A key to an effective design of metamaterials for any application is a thorough understanding of their underlying structure-property map. As it can be deduced, it is more challenging to do than for conventional materials, as the resulting macroscopic properties depend not only on the bulk material itself but also on the introduced microscale architecture. Therefore, it is important to make a clear distinction between any properties stemming purely from the material's intrinsic nature, i.e. *base material properties*, and the macroscopic *effective material properties*, which also take into account any intermediate structures. An example of an effective material property is previously introduced relative density. In other words, for metamaterials, the structure-property map refers directly to the link between the effective material properties and the introduced intermediate-level architecture. Once this link is fully understood, one can use it to efficiently maximise or tune the desired metamaterial functionalities - for example, in designing bone implants such goal can be to perform anisotropic stiffness matching.

One possible way to categorize mechanical metamaterials is with respect to their topology type. Some of the most commonly encountered metamaterial lattices are based on truss elements, plates or shells. Metamaterials can be distinguished also on the basis of their unique properties. This division identifies, for example, super-elastic materials. An example of property classification would also be a collective of ultra-light, ultra-stiff metamaterials reported by Zheng et al. These materials are characterised by an almost constant stiffness per unit mass density, even at extremely low densities [15]. In other words, the stiffness of these materials varies linearly with density, while for the majority of the conventional porous structures, especially when the relative densities drop below 1%, the elastic modulus varies quadratically (or exhibits an even stronger scaling factor) with density; similar situation occurs for the strength-density relationship [15]. Another noteworthy metamaterial subtype is the auxetic materials, i.e. materials that have a negative Poisson's ratio. Several studies described the advantages of auxecity specifically for bone tissue replacement applications. Auxetic structures reportedly have the potential to accommodate any fluctuations in the bone volume, hence minimizing the risk of implant/scaffold loosening. Moreover, their synclastic curvature allows for the relatively good adjustment of the structure to irregular bone defect shapes. [16] Auxetic metamaterials will, however, not be elaborated upon in this work. As of today, the abundance of research conducted on mechanical materials makes it impossible to cover all possible subgroups and subtypes exhaustively. The focus of the work will be kept on the newly emerging class of spinodal and spinodoid metamaterials. Studying spinodal metamaterials for usage in bone substitutes, on the other hand, is a novel concept; however, their reported potential to resolve some of the shortcomings in the current BTE solutions was considered worth delving into.

2.2.1 Additive Manufacturing Routes

In recent years the field of additive manufacturing (AM), also commonly referred to as 3D printing, has grown substantially. A surge in its popularity can be attributed to its unique processing characteristics, through which it is possible to achieve part properties difficult to obtain with conventional manufacturing. It has to be noted, however, that while for many specific applications, AM is very favourable, it should be treated as a processing strategy complementary to traditional manufacturing, rather than a solution that would replace it completely. AM approach allows for the fabrication of structures with virtually any shape, and with a very small feature resolution. The individual part production is relatively fast; it is also efficient in terms of material usage and independent of the geometrical complexity of the produced part. Although it was initially developed for rapid prototyping, direct digital manufacturing (DDM), which is the AM production of end-use parts, also gradually became more popular. Design for DDM excludes the necessity for dies, moulds or fixtures, decreases the production cycle time and involves easily reusable, adjustable digital datasets. While DDM is not suitable for mass production, it is a very feasible manufacturing approach for mass customization of end-use products - one example of such being patient-specific, tunable bone implants and scaffolds.
Overall, additive manufacturing provides an efficient approach for producing highly complex parts with sufficient mechanical properties. However, AM also has various limitations, some of which have already been introduced for specific manufacturing routes. More broadly, all parts produced by 3D printing have rather poor repeatability, even if they are built using the same machine. They are also inherently anisotropic, porous, and are usually, at least to some extent, affected by thermal stresses. All these factors are inevitably linked to a high defect presence, and consequently, a fall in the mechanical performance of the part. Additionally, the scalability of additive manufacturing processes remains a challenge. While AM techniques such as DLW-2PP allow for achieving very high feature resolution, generating multiscale samples, i.e. large volume parts that still contain microscale features, is not straightforward. These issues could potentially be addressed by a new generation of manufacturing oriented on the self-assembly processes, which will be discussed in the later part of the report.

2.3 Spinodal decomposition

As discussed in the previous sections, there are two substantial challenges in the design and optimization of metamaterial-based lattices. Firstly, the theoretically predicted mechanical performance of the periodic structures is rarely achieved due to their sensitivity to imperfection. Defect presence in those topologies is, in turn, inherently linked to the additive manufacturing techniques used to build them. Secondly, the scalability in the production through the AM routes is not straightforward and achieving structures with larger volumes, which will at the same time possess features on the micro- and nanoscale, remains a challenge. Additionally, the ability to efficiently introduce anisotropy into the implant/scaffold design space, or taking it a step further, the construction of functionally graded structures, is a desirable objective. It is important to note, however, that for conventionally truss-based and TPMS topologies, the extent to which anisotropy can be implemented is limited by the requirement for periodicity. In an attempt to resolve the shortcomings of the periodic strut-based and shell-based metamaterials, various researchers have sought inspiration from naturally occurring structures such as the

trabecular bone itself. One of the objectives was to search for topology in which locations of high-stress concentrations, such as nodal points in truss-based lattices, are not present. In recent years, multiple research groups have shifted their focus towards *spinodal* structures, which were first studied as early as the 1960s. Their stochastic nature and the possibility to fabricate them through a process of self-assembly results in the potential to resolve both the problem of susceptibility to symmetry-breaking defects and the scalability issue.

2.4 Metamaterials based on spinodal decomposition

There are two substantial challenges in the design and optimization of metamaterial-based lattices. Firstly, the theoretically predicted mechanical performance of the periodic structures is rarely achieved due to their sensitivity to imperfection. Defect presence in those topologies is, in turn, inherently linked to the additive manufacturing techniques used to build them. Secondly, the scalability in the production through the AM routes is not straightforward and achieving structures with larger volumes, which will at the same time possess features on the micro- and nanoscale, remains challenging. Additionally, the ability to efficiently introduce anisotropy into the implant/scaffold design space is a desirable objective. However, when designing truss-based and TPMS topologies, the extent to which anisotropy can be implemented is still limited by a requirement for periodicity. In an attempt to resolve the shortcomings of the periodic strut-based and shell-based metamaterials, various researchers have sought inspiration from naturally occurring structures such as the trabecular bone itself, in which locations of high-stress concentrations, such as nodal points in truss-based lattices, are not present. In recent years, some research groups have shifted their focus towards *spinodal* structures, which were first studied as early as the 1960s. Their stochastic nature and the possibility to fabricate them through a process of self-assembly results in the potential to resolve both the problem of susceptibility to symmetry-breaking defects and the scalability issue.

2.4.1 Spinodal decomposition - physical significance

Before discussing the concept of spinodal metamaterials, a physical mechanism of spinodal decomposition shall be introduced. In principle, spinodal decomposition describes the process of near-instantaneous phase separation of a single-phase mixture, which spontaneously occurs without a nucleation barrier.[18, 19] An example that can be used to help visualize the mechanisms of spinodal decomposition is a uniform solution of the two polymer blends, A and B.
The important physical parameters investigated are the Gibbs free energy of mixing (G_{mix}) and the Gibbs free energy of the individual components G_A and G_B. In principle, the considered system is completely miscible if the free energy of mixing is never greater than the free energy of any two possible co-existing phases. In other words, if G_{mix} is always more negative than G_A and G_B at any composition and any temperature, the two individual components will continue to coexist in a single-phase solution. However, if for a given temperature there is a concentration value or concentration range, for which G_{mix} is more positive than the free energy G_A and G_B, at these concentrations the A-B system is no longer miscible. Figure 2.1 schematically presents a simple phase diagram and a Gibbs energy vs. concentration plot constructed for such a non-miscible, binary system. In the upper drawing (Figure 2.1a), the phase change boundaries were drawn for two different

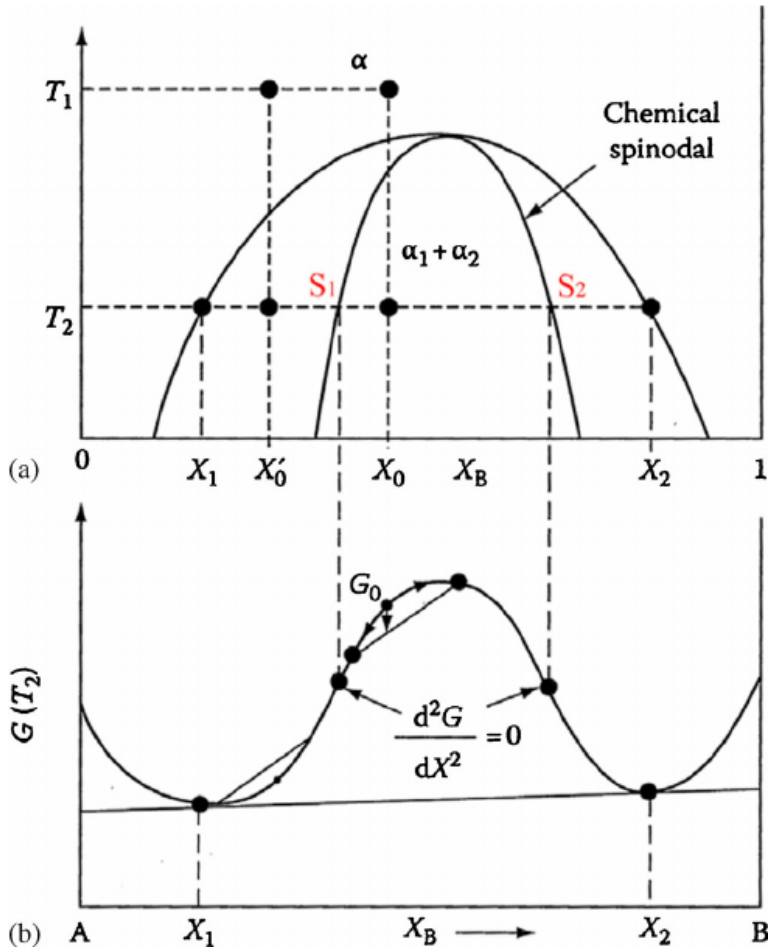

Figure 2.1: The plots showing the relationship of the free energy of an arbitrary polymer blend mixture with the constituent phase composition and temperature. The region in which the (chemical) spinodal decomposition occurs is indicated. [17]

temperatures T_1 and T_2, where $T_1 > T_2$, at different concentrations of constituent B (from 0 to 1). The outer contour of the plot marks the phase boundary, above which the two polymer blends are miscible and the system is stable. For example, a mixture containing constituent B at a concentration of X_0 will be in a stable state at temperature T_1. The inner contour of the plot, labelled as chemical spinodal, marks the region of the plot where the system is fully unstable. Below the phase boundary and above the spinodal line lies the metastable region. [19]
This upper plot is then mapped on the lower drawing (Figure 2.1b), where Gibbs free energy specific for the temperature T_2 is plotted against the phase concentration. For a given temperature, e.g. T_2, the phase separation through the spinodal decomposition takes place for all the concentrations that fall in the region where the Gibbs energy curve is concave, i.e. between the inflexion points. At these points, the second derivative of G_{mix} is equal to zero, as it was marked in Figure 2.1. This composition range is commonly referred to as a miscibility gap. Referring back to the upper plot, the unstable and metastable

regions comprise together the miscibility gap, and it is in this region that the system changes from a single phase to a double phase.
In principle, each physical system tends to evolve and ultimately strive to reach thermodynamic equilibrium. For a system such as that considered above, this is obtained by the coarsening of the separated topologies; through which the energy term corresponding to the interfacial tension between the two phases is gradually becoming smaller. The resulting spinodal decomposition, occurring in the miscibility gap, is a diffusion-driven process; the direction of the diffusion, however, is against the concentration gradient. Due to the strong thermodynamic effect, it is more energetically favourable for the particles to move "uphill" in terms of concentration, hence the term *uphill diffusion* is used.

The time needed for this transition to reach the equilibrium phase is characteristic of each mixture. Overall, the period of the phase separation through the spinodal decomposition in which the individual phases have not yet reached the equilibrium concentration is commonly referred to as an "early stage" of demixing. This description relates to the terms "early" and "late" spinodals, which would be used later in the work. [20] In more general terms, the kinetics of the spinodal decomposition can be described by solving the Cahn-Hilliard equation. In short, this equation describes how the concentration of one constituent phase changes in time, provided that the local concentration of the phase is known. Key constituents of the Cahn-Hilliard equation are the parameters related to the fluid concentration, c, and to the diffusion coefficient, which is often represented by a mobility constant, M. After linearization, the Cahn-Hilliard equation takes a form:

$$\frac{\partial c}{\partial t} = M\frac{\partial^2 f}{\partial c^2}\nabla^2 c - 2M\kappa\nabla^4 \tag{2.1}$$

Here, κ is related to the interfacial energy, while the function *f(c)* is the homogeneous free energy density term. In his separate work, Cahn demonstrated that the composition field formed at the early stages of spinodal decomposition can be expressed as a superposition of standing sinusoidal waves, which are of specified wavelength and amplitude, but which are random in terms of their phase and direction. Mathematically, this translates to a Gaussian random field (GRF), and it can be written as follows:

$$f(x) = \sqrt{\frac{2}{N}}\sum_{i=1}^{N}\cos(\beta \boldsymbol{n_i}\cdot\boldsymbol{x} + \gamma_i) \tag{2.2}$$

Here *f(x)* stands for the field, $\boldsymbol{x}$ represents the position vector, N denotes the number of waves considered, $\boldsymbol{n_i}$ corresponds to the direction of the ith wave, and γ_i refers to its phase angle, which for isotropic systems are, in principle, random and independently sampled variables [21, 5].

2.4.2 The strategies of the topology generation

Thus far, the aspect of the topology generation for metamaterial design and manufacturing has not been discussed; it is nonetheless an important stage of the process. Major advances in machine learning in the past years, especially in the field of deep learning and neural networks (NNs), have allowed for topology generation to become much more efficient, and hence for the available design space to be largely expanded. Some publications have

previously described attempts to use NNs, for example, to optimise the route for truss topology prediction [22]. A similar strategy has also been demonstrated also for structures based on spinodal decomposition [5]. The results turned out to be promising in terms of anisotropy generation and construction of spatially graded structures. These innovations could, consequently, be very relevant for solving problems such as one described earlier related to bone substitute biomaterials.

As outlined in the previous subsection, spinodal topologies can be generated by modelling the equations governing the underlying kinetics of the spinodal decomposition. This, however, most often implies the necessity of using a computationally intensive phase field method for simulating the Cahn–Hilliard process of phase separation [5]. An alternative, machine learning approach was demonstrated by Kumar et al, through which it is possible to generate *spinodoid topologies*, i.e. topologies that closely resemble the spinodal microstructures. In an earlier study, Soyarslan et al. already provided a method of generating such spinodal-like topologies, which were based on Gaussian random fields (GRFs) resulting from a superposition of standing sinusoidal waves. However, their work was only focused on the isotropic structures [21]. As a point of departure from the isotropy, the work by Kumar et al. utilises anisotropic GRFs based on a simple parametrization, which effectively enabled an expansion of the design space to include anisotropic topologies. Overall, the primary approach to navigating the relationship between the structure and the mechanical properties of metamaterials is based on a forward design, i.e., the material properties are obtained from a previously determined microstructure. The inverse strategy, where the specific topology is identified based on the sought-after mechanical properties, is more universal, as it can be applied to virtually any constituent material and any design parameter configuration. It is also very promising for applications such as spatially graded bone implants or scaffolds, which could possibly be tuned to accommodate patient-specific anatomy. However, by default, more than one microstructure can be characterised by the same mechanical properties. This renders the inverse design problem ill-posed and more challenging to solve - it is often attempted simply by a trial and error [5]. The potential solution was demonstrated in the aforementioned study by Kumar et al. They demonstrated the usage of a deep neural network-based method, which can be effectively trained on a large training dataset containing information about the specific design parameters and the corresponding stiffness values, extracted using FEA software. The generation of a sufficient number of data points necessary for the model training is enabled by the previously described, efficient GRF-based description of the spinodoid structures. The proposed method follows two steps. First, the inverse model uses the designated stiffness as input and produces the output design parameters corresponding to a specific topology, using the GRF equation as a basis. Then, the generated design parameters are taken as input in a forward model, which subsequently incorporates FEM to compute the matching stiffness and, consequently, to verify the predictions from the inverse model. On the whole, due to the strong dependence of the stiffness on the $\overline{\rho}_0$, the inverse model succeeds in recovering the corresponding data for a specified stiffness value.

The advantage of the demonstrated machine learning framework is that it can be used to attain functional grading. Specifically, the inverse design model is capable of producing a set of independent GRFs, with each locally conforming to the designated anisotropic stiffness, which can then be easily interpolated. The visualisation of the functionally graded structure is shown in Figure 2.2.

A continuation of the work by Kumar's group was published by Zheng et al. In their paper, they demonstrated a framework for multiscale topology optimization. This framework was reported to be applicable for the optimisation of the macroscopic mechanical behaviour in

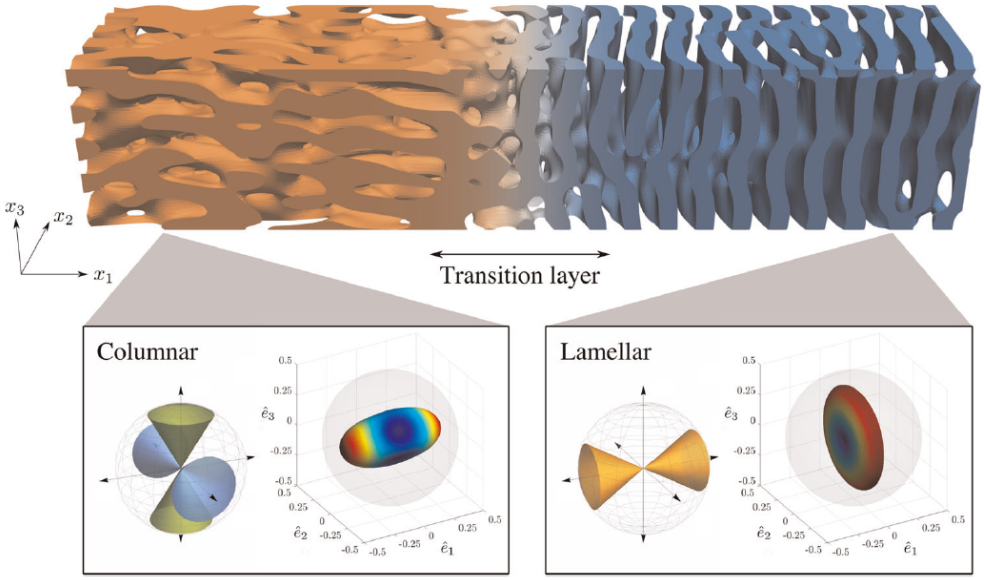

Figure 2.2: An example of a spatially graded architecture, combining columnar and lamellar spinodoid topologies (marked with orange and blue). The elastic surfaces stemming from the two underlying GRFs are shown with their design parameters, reproduced from [5].

an elastic regime, realised by the tuning of spatially varying spinodoid microstructure which makes up the body. The spinodoid topology was chosen due to its capability of introducing the functional grading (as shown previously in Figure 2.2) and hence, of achieving elastic anisotropy. The spinodal topologies also require only a small set of design parameters linked to the intrinsic GRF. The underlying principle of this method is that instead of utilising less efficient homogenisation in the microscale, it makes use of a data-driven surrogate model based on deep neural networks, which is capable of mapping the design parameters onto the fourth-order stiffness tensor in a very efficient manner. The benefits of this approach include making the topology optimisation significantly faster, as well as that it gives an easier and less costly insight into the exact sensitivities, which are needed in the process required for gradient-based optimization. Although the analysis by Zheng et al. was done for skeletal spinodoid topologies with $\bar{\rho}_0$ >30, which are arguably worse in terms of their mechanical performance, it has been reported that the study can be extended to include the more promising, shell-based topologies.

2.4.3 Mechanical characteristics of spinodal metamaterials

Having described the process of spinodal decomposition, the specifications of the spinodal metamaterials can be outlined. The spinodal decomposition of a mixture leads to the formation of two distinct, stable phases, which make up a bi-continuous topology. Those phases are partitioned by a non-self-intersecting surface, which, as in the triply periodic minimal surfaces, has approximately zero mean curvature.[5, 18] Analogously to TPMS lattices, the ensuing spinodal topologies can be divided into the shell and skeletal (solid) topologies. As with the TPMS metamaterials, solid spinodal topologies are formed by the

removal of one of the formed phases, while shell-based spinodals are formed upon the removal of both constituent phases and preservation of the interface, of a finite thickness, only.[23]
In recent years, several publications which aimed to investigate the mechanical behaviour of spinodal topologies emerged. Hsieh et al. in their early study performed numerical and mechanical testing of a range of spinodal topologies. Their tests included both the shell and the solid structures with varied relative densities, which have been exposed to a uniaxial compression simulation in finite element analysis software. The FEA modelling was followed by performing an in-situ uniaxial compression test on 2-photon polymerization DLW printed specimens.[18] It has to be noted, however, that only the fully isotropic behaviour of the structures was examined, and that the structures were only tested in one loading mode. Both the experiments and the simulations indicated that the solid spinodal topologies, which had densities between 30 and 70%, exhibit a rather poor scaling of Young's modulus and yield strength with the relative density. However, the shell-based spinodal structures were able to achieve a remarkable stiffness scaling ratio proportional to $\overline{\rho}_0{}^{1.2\text{-}1.4}$. The reported scaling relationship is coming close to the theoretical predictions for the most favourable stiffness/yield strength scaling for isotropic metamaterials. [18] The group has also reported that the spinodal shell topologies had a very good tolerance for the presence of defects, and therefore they were significantly less sensitive to buckling-induced failure. Buckling, as described in an earlier section, was the main failure mode, particularly for the non-hollow truss-based lattices at ultra-low densities, which severely limits the strength in these structures in comparison with the theoretically predicted values. In the

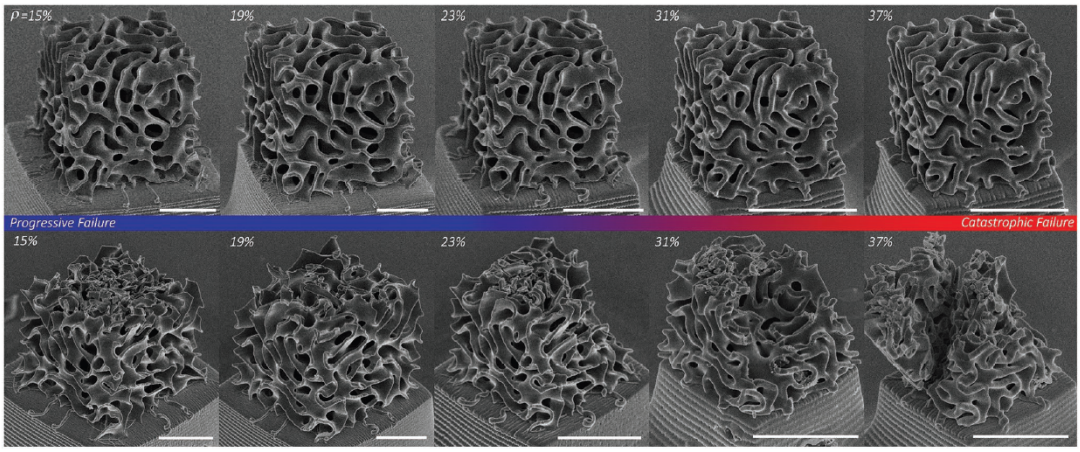

Figure 2.3: Glassy carbon spinodal shell-based topologies with varying relative densities ($\overline{\rho}_0$), manufactured via 2PP-DLW and pyrolysis. Top and bottom images show the structures before and after initial failure during uniaxial compression. The distinct transition from progressive to a catastrophic failure mechanism is shown for increasing relative density. Scale bars are 5 um, reproduced from [24]

.

subsequent study, Guell et al. manufactured the spinodal shell-based structures out of IP-Dip photoresist on silicon substrates, also by using two-photon direct laser writing. The printing process was followed by high-temperature pyrolysis to transform the cured photoresists into glassy carbon. The resulting structures had relative densities in a range of 15–40% and features down to 170 nm. As in the previously described study, the produced

samples were tested under uniaxial compression, and their stress-strain behaviour was recorded. The nanostructured and tunable spinodal topologies were reported to exhibit stretching-dominated behaviour, resulting in very favourable stiffness and strength scaling with a relative density, significantly better than that of bending-dominated stochastic foams. The high strength and stiffness recorded were comparable with values commonly reported for strong, yet brittle nanolattices. At the same time, the tested specimens were capable of energy absorption as high as 200 kJ per kg. Akin to TPMS lattices, spinodal topologies showed an approximately homogeneous strain distribution upon loading.[24]
The most critical finding of this study was that the tested samples exhibited non-catastrophic, layer-by-layer-type failure for densities under approximately 25%. Figure 2.3 shows five samples with increasing relative density $\overline{\rho}_0$ before and after they underwent the mechanical testing. An evident transition from a progressive to a catastrophic failure is seen with an increase in $\overline{\rho}_0$. To complement the mechanical testing and further investigate the failure mechanisms, a finite element analysis was carried out. It was found that optimising the ratio of the shell thickness to the curvature radius in spinodal topologies can impede the propagation of cracks oriented along the loading direction, and hence prevent catastrophic failure during compression. Instead, the propagation of transversely oriented cracks was promoted, resulting in a progressive failure mode. By comparison, this mode of desirable, controlled failure, characterised by high-stress plateaus, is not easily achievable for truss-based structures.

A promising work inspecting the properties of spinodal topologies was also carried out by Valdevit et al. The research group examined the performance of spinodal topologies in interpenetrating phase composites (IPCs). IPCs, contrary to the more commonly manufactured composites, do not possess a dispersed reinforcement phase but include it in a form of continuous topology. The study focused on manufacturing and testing solid and shell spinodal IPCs, as well as two other, well-known reinforcement topologies: the octet-truss lattice and Schwarz primitive TPMS. Firstly, the data for the solid and shell spinodal IPCs were compared. The results were aligned with the findings from previously outlined publications and shown that the IPCs with shell-based reinforcement were unrivalled in all the metrics tested. Their superior properties were more evident especially at smaller reinforcement volume fractions, due to the minimized stress concentrations and general stretching-dominated behaviour in the shell topologies. At increasing reinforcement volume fractions, and hence also increasing topological resemblance between the two structures tested, their mechanical performances converged. Therefore further tests were carried out only on the shell spinodal IPCs.
In the successive part of the study, a comparative mechanical behaviour analysis of the three distinct IPCs was carried out. All three structures displayed very similar stiffness and yield strength, the IPC with a spinodal reinforcement showed the best performance in terms of damage resistance and exhibited less catastrophic failure, especially at higher V_f of the reinforcement. These superior properties were ascribed to the uniform distribution of stresses, but also a comparably larger surface area for a specific V_f of the reinforcement phase. Additionally, the departure from the periodicity and the unique character of the spinodal topology contribute to the local impediment of crack propagation, and the ability to continuously provide mechanical support even after partial failure in the structure.

2.4.4 Self-assembly based manufacturing

Spinodal structures can be computationally generated and produced using commercially available additive manufacturing methods, for example, SLM or EBM. [12] Techniques such as direct laser writing combined with two-photon polymerisation have also been used, as highlighted in the previously reported studies. Taking a step further, Portela et al. practically demonstrated a feasible way of manufacturing the spinodal topologies through the process of self-assembly. A great advantage of this approach over the conventional additive manufacturing processes is its potential for scalability. The researchers reported successful fabrication of the materials architected in a nanoscale, which had features ranging from nanometers to centimetres. Specifically, the bulk volume of those structures was on the of cubic centimetres, the internal pore dimensions were of the order of tens of micrometres, while the thickness of the walls was in the order of tens of nanometers. The

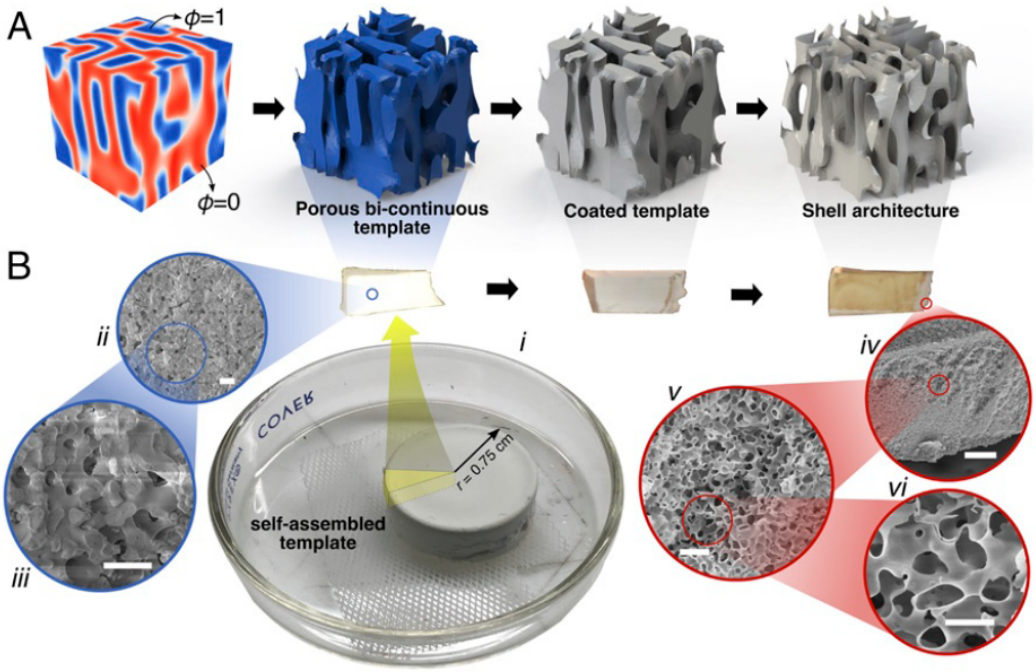

Figure 2.4: Self-assembled nanolabyrinthine shell-based material. (A) Schematic of the fabrication process starting with spinodal decomposition of an epoxy resin emulsion (blue) and PEG (red). After the extraction of PEG, the emulsion is thermally cured to produce a porous bicontinuous template. The template is then conformally coated with ALD Al_2O_3, which after removing the epoxy phase via O_2 plasma ashing, composes the resulting nanolabyrinthine shell architectures. (B) Photograph of a self-assembled porous epoxy disk fabricated using the process described above, together with the SEM micrographs of a wedge extracted from the disk. Scale bars: Bii and iii, 10 um; Biv 100 um; Bv 10 um; Bvi 5 um, adapted from [25]

self-assembly method for the production of the spinodal topologies, which Portela and his research group developed, is shown in Figure 2.4. The key steps included the initial

spinodal decomposition of the epoxy resin emulsion and polyethylene glycol (abbreviated as PEG). PEG is then removed, leaving a solid spinodal topology formed by the epoxy resin phase only. This remaining phase is reported to be fully interconnected and isotropic, while its relative density upon polymerization was shown to be approximately 44%. In the subsequent step, the structure is conformally coated with alumina (Al_2O_3) using an atomic layer deposition process. Finally, plasma ashing is utilised to remove the epoxy resin, leaving out only the nanolabyrinthine, shell-based Al_2O_3 topology. In the latter part of the study, after demonstrating the self-assembly of spinodal topologies, the researchers performed a systematic exploration of a parameter space on the computationally generated spinodal topologies. Subsequently, a two-photon lithography DLW using IP-Dip photoresist, followed by deposition of ALD alumina coating and selective FIB etching to remove the photoresist was done to manufacture specimens representative of the modelled spinodal topologies. Then, the uniaxial compression was performed and simulated on the structures along the primary axial directions. The numerical analysis shows that the curvature of the self-assembled shell-based structures can lead to a nearly-optimal scaling of the stiffness with the relative density. The tested spinodal structures have also shown exceptional properties in terms of energy absorption, and, which was largely the focus of the study, mechanical resilience, as demonstrated through their recovery after undergoing repeated nonlinear compression. [23]

2.4.5 Potential of spinodal topologies for bone biomaterial applications

Up until this point, spinodal topologies were analysed mostly with regard to their mechanical performance. In this section, the focus will be brought to the context of their usage as biomaterials for bone regeneration. To start with, we will refer back to the previously cited work by Kumar et al. In the latter part of their publication, the group presented an example application for their topology generation strategy in the design of a spinodoid-based synthetic bone, using the bovine trabecular bone data. The relative density and direction-specific stiffness of the bone specimens were obtained experimentally. Then, assuming isotropy in the bone material, the acquired variations in the directional modulus were taken as a query in the simulation, and the inverse NN model was implemented to generate corresponding structures and their properties. The analysis showed that the i-NN model predicted the relative densities and stiffnesses of the samples with good accuracy, while the background information regarding the bone was not disclosed during the learning period. The generated columnar spinodoid structures resembled the morphology of the real bone, having features oriented along the loading direction resembling the human trabeculae alignment. It has to be noted, however, that the normal–shear coupling terms in the experimental stiffness tensor caused minor discrepancies between the compared stiffness values.

Hsieh et al. in their recent work compared the potential of three metamaterial topologies for long bone implant applications. They performed a numerical analysis on an octet-truss lattice, a Schwartz's primitive TPMS lattice, and a non-periodic spinodal shell topology. Three implant materials, specifically a titanium alloy, a CoCr alloy and stainless steel, and three values of relative density ($\overline{\rho}_0$ of 0.1, 0.2 and 0.3 respectively) were analysed for each structure. Each topological model was input into FEA software as a composite system made out of two elastic constituents, i.e., the implant material and the surrounding soft matrix representing the cartilage tissue. It is important to point out here, however, that human cartilage tissue is naturally viscoelastic, hence modelling it in an elastic regime is

naturally burdened with some level of inaccuracy. All models were loaded in displacement-controlled compression, and the resulting stress and strain field data were extracted. Then, the performance of each topology has been evaluated in terms of the effective Young's modulus, and the load safety factor, which provides an insight into the implant's fatigue resistance in service. The analysis also compared the specific surface area of the bone/implant interface for each model and introduced a novel, scalar parameter which could help to indicate a capacity to promote bone growth. This metric was based on the analysis of the strains present in the peri-implant soft tissue and was closely linked to the osteogenic index. The results showed that for all the topologies and all the metallic

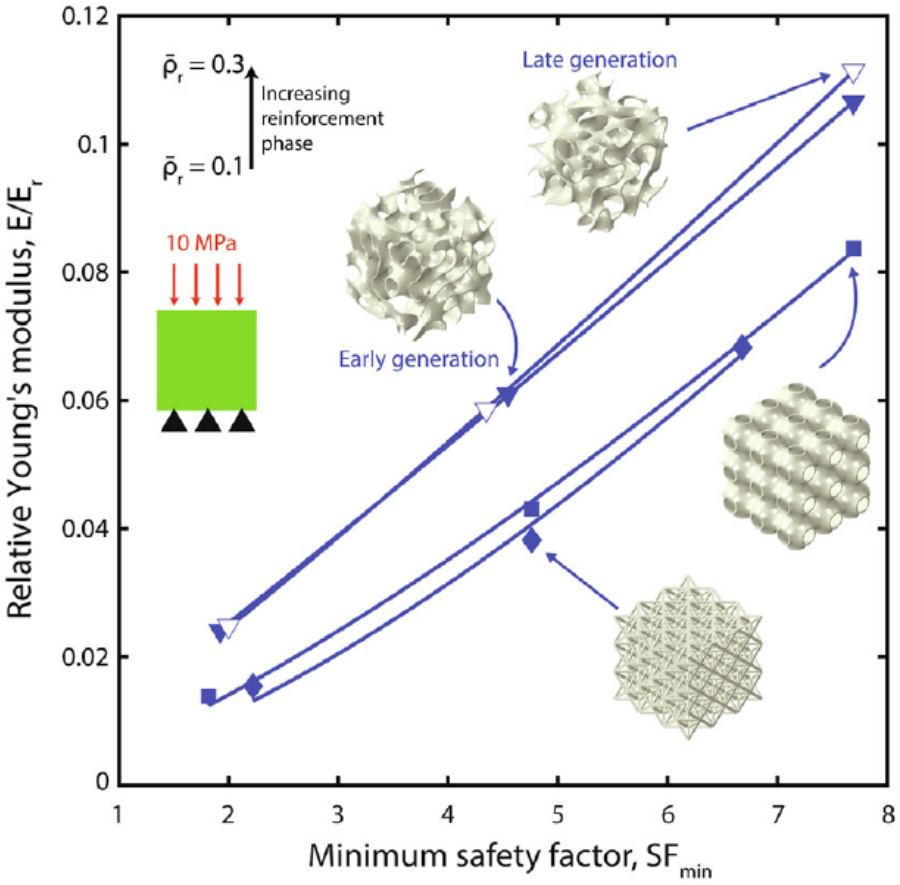

Figure 2.5: Relative Young's modulus versus minimum safety factor for octet, primitive, early- and late-generation spinodal implants with relative densities of 10%, 20%, and 30%, reproduced from [12]

biomaterials tested, it is possible to tune the structure's specific stiffness to match the stiffness of the bone. Spinodal topologies were reported to have the smallest safety factor for the same given loading conditions and target stiffness, ultimately requiring less material to fulfil all the design criteria. For shell-based topologies in general, the stiffness and the specific surface area were shown to be decoupled, allowing to achieve the desired stiffness while minimizing the impact on the surface area. Figure 2.5 shows the relationship

between the minimum safety factor and the relative elastic modulus. In addition to the advantages shown by shell-based topologies, the spinodal structures were also shown to have an exceptionally good prediction in terms of their fatigue life.
The surface area in the shell-based structures was also reported to be nearly shell-thickness independent, and they have demonstrated a significantly better ability to promote bone growth compared to the strut-based lattices. It has to be noted, however, that due to a decrease in volumetric strain early-generation spinodals showed the lowest bone growth potential out of all the shell-based topologies.

In their study considering the bone morphology, Callens et al. also discussed the potential of the examined morphology analysis tools for looking at various structures considered for bone replacement, in order to assess their similarity to the bone tissue. The research group performed that analysis for an octet-truss lattice, gyroid TPMS lattice and a spinodoid topology. For the octet-truss structure, the curvature spectrum was shown to be limited - its constituents were primarily cylindrical components, while the non-zero Gaussian curvature was observed only at the nodal points. The gyroid TPMS lattice, often considered one of the most suitable bone-replacement topologies, was shown to exhibit a vanishing mean curvature and a negative/zero Gaussian curvature along the surface, showing a rather narrow, not the most favourable ISD spectrum. However, the analysis of a spinodoid structure showed a broader curvature spectrum, which bore a closer resemblance to the natural bone. Still, a symmetry of the ISD spectrum was observed for this stochastic structure, which was not present in the trabecular bone spectrum analysis.[26] Nevertheless, it is important to note that the ISD analysis applied here by Callens et al. is only one of the measures to gauge the bone-mimetic potential of the selected metamaterial topologies, and various other factors, such as mass transport or mechanical properties, need to be taken into account.

2.4.6 Future studies

Until now, this report aimed to provide an overview of the requirements and challenges in the design of biomaterials for bone regeneration, focusing specifically on the potential of metamaterials. The presence of points of high-stress concentrations, linked to short fatigue life and increased risk of failure, emerged as a limitation in truss-based structures. The attention was hence brought towards the novel spinodal metamaterials, and some early studies on their mechanical performance, as well as some evaluation of their suitability for bone biomaterials, were presented. Smooth, stochastic and multiscale topology which can be realised through self-assembly-oriented manufacturing provides a potential solution to the concerns posed by the previously introduced periodic metamaterials. The developments in topology generation strategies also lead to many opportunities for creating anisotropic and spatially graded structures. As a result, spinodal-based metamaterials could become a viable means of achieving tunable, easily reproducible biomaterials with long fatigue life and optimal morphological properties. Nevertheless, although spinodal metamaterials have shown promising qualities, many more tests need to be carried out to assess their actual potential for bone implant applications. This final section aims to outline some of the possible future research directions related to, among others, spinodal topology generation, mechanical behaviour, manufacturing and biocompatibility.
With regard to the topology generation strategies presented by Kumar et al., the accuracy of the simulations may be further improved in the future by including additional data

training of the inverse model; or by finding alternative means to expand the existing training datasets. The reported analysis on designing a synthetic spinodoid-based model could be used as a starting point, and future works could potentially go beyond the bone isotropy assumption and apply it to more complex models. Further studies on developing anisotropic and functionally graded structures are also a promising research route.
Thus far, the majority of tests on the mechanical behaviour of the spinodal structures involved only the tests in the uniaxial compression. The real-life application of the implants and scaffolds would eventually require testing in more complex loading modes, aiming to approximate the load distribution in the patient's bone. Most studies have also focused on the elastic behaviour of those structures only, while bone tissue itself exhibits a more complex mechanical response. Further studies could hence extend the simulations and tests of the spinodal and spinodoid topologies to include matching the design parameters in the viscoelastic and viscoplastic regimes. Subsequently, tests on a range of strain rates can also be included. Additionally, except performing the test related predominantly to verifying the stiffness or yield strength of the structures, it would be beneficial to explore other parameters, for example, the non-linearity of the loading, fatigue behaviour, and ductile damage criteria among many others. [8] The complementary model simulations, in turn, could possibly be improved by replacing or supplementing the finite element modelling with methods such as Fourier-based spectral formulation (FFT). Finally, future mechanical tests can also be carried out on the range of other materials, including also biodegradable biomaterials and their behaviour in the future.
Further work can also be done on self-assembly manufacturing for producing bone replacement materials. The work by Portela et al. outlined earlier brought about new prospects in bone scaffold and implant design - scalable structures with micro- and nano-scale features could be used to mimic bone's hierarchical architecture, and the resulting increase in the specific surface area in the structure could lead to improved osteogenic properties.[12] The process demonstrated for alumina could potentially be extended to explore other ceramics, such as hydroxyapatite. Future works could also, hopefully, explore the assembly of anisotropic structures.
Incorporating spinodal topologies into interpenetrating phase composites is another possibility in bone biomaterial development. IPCs constructed for the purpose of bone regeneration have already been demonstrated in previous studies, e.g. Okulove et al. presented a way of manufacturing Ti-based metal-polymer nanocomposites with the distinct phases being topologically interconnected.[27] A major advantage of that approach could be an improved ability to tune the mechanical properties, as well as incorporating multiple materials into the structure. Using the results from the cited IPC study by Valdevit et al. for further work on spinodal shell reinforcements in IPCs for synthetic bone substitutes can be a promising research direction.
Naturally, one cannot forget about the necessity of eventually performing tests in a biological environment. Metrics like osteogenic index, or other proposed indicators such as the one introduced by Hsieh et al., helpful in the prior analysis can also be further developed. Nevertheless, they should be treated only as a preliminary method before the long-term *in vitro* and *in vivo* tests are carried out. Studying parameters like bone ingrowth rate or osteoblasts proliferation, among others, is crucial to verify the final success rate of spinodal metamaterials in bone regeneration treatment.

On the basis of the aforementioned knowledge gaps, the main objective of the thesis can be defined. The main focus of this work was chosen to be the computational analysis of the mechanical behaviour of the spinoidoid structures in a viscoelastic regime. First, the general concept of viscoelasticity shall be introduced.

2.5 Viscoelasticity

As mentioned in the previous section, studies on spinodal topologies have primarily been conducted within the elastic regime. The elastic regime, by definition, assumes the conservation of energy during material deformation. In other words, the strain energy is fully recoverable, and the material's mechanical behaviour remains independent of the strain rate. However, many real-life materials deviate from perfect elasticity and display varying degrees of viscous behaviour. Materials that exhibit both elastic and viscous behaviours are known as viscoelastic materials. Viscosity introduces energy dissipation linked to material deformation and results in a dependence of mechanical behaviour on the strain rate. Hence, if a constant strain is applied on the elastic material, the material shows a constant stress response; while for viscoelastic material, the same strain would yield a time-dependent stress response.
Modelling materials within a viscoelastic regime offers a more accurate analysis of a wide range of materials, including commonly used polymers. This is especially relevant when exploring the potential applications of these materials for spinodal-based structures. In the realm of bone biomaterials, notable examples of synthetic polymers like PLLA, PEEK, and PGLA are employed in the fabrication of bone scaffolds.

Two common experimental tests are performed on viscoelastic materials. The first involves the phenomenon known as creep, whereupon applying a constant load on the measured strain changes over time. Another mechanical test relates to stress relaxation, in which viscoelastic material under constant strain shows a decreasing stress response. The change of the stress in time in response to constant deformation defines a concept of a relaxation modulus E_r, analogous to Young's modulus in an elastic material:

$$E_r(t) = \frac{\sigma(t)}{\varepsilon_o} \tag{2.3}$$

Similarly, creep modulus can be defined as a ratio of strain changing with time in response to constant stress:

$$D_c(t) = \frac{\varepsilon(t)}{\sigma_0} \tag{2.4}$$

In principle, viscoelastic materials can be represented using various constitutive models, which are usually schematically represented by a combination of springs (elastic contribution) and dashpots (representing the viscous components). Visually, different viscoelastic models can be thought of as different ways in which the springs and dashpots are connected with each other. The two simplest rheological models are the Maxwell model, in which a single elastic element and a single viscous element are connected in series, and the Kelvin-Voigt model, where these elements are connected in parallel. The scheme of these two models is illustrated in figure 2.6. The E and η represent the elastic modulus of the elastic element, the viscosity of the viscous constituent. In this case, E is equivalent to spring constant k in Hooke's law, and η stems from the expression of a stress response in a Newtonian fluid, i.e. $\sigma = \eta\dot{\varepsilon}$. The general equation governing the deformation of the simple Maxwell model can be written as follows:

$$\frac{\dot{\sigma}}{E} + \frac{\sigma}{\eta} = \dot{\varepsilon} \tag{2.5}$$

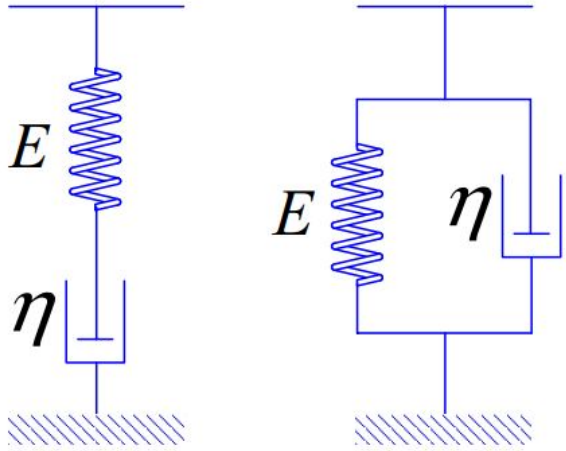

Figure 2.6: A schematic of two simplest viscoelastic models, reproduced from[28].

where σ and $\dot{\sigma}$ are the stress and the time derivative of stress, while $\dot{\varepsilon}$ stands for the strain rate. The equation of motion for Maxwell model:

$$\frac{d\varepsilon}{dt} = \frac{1}{E}\frac{d\sigma_E}{dt} + \frac{\sigma_E}{\eta_E} \tag{2.6}$$

OR another form of motion equation:

$$\frac{d\gamma}{dt} = \frac{1}{G}\frac{d\sigma}{dt} + \frac{\sigma}{\eta} \tag{2.7}$$

A simple Maxwell model can be extended into its generalized form to achieve a more versatile representation of a viscoelastic material. This can be achieved by taking N pairs of springs and dashpots and connecting them in parallel, as shown schematically in figure 2.7. If this model is subjected to loading, the global stress of the model is a sum of the individual stresses experienced by each Maxwell element (one spring and one dashpot), and the strain value exerted on each of them is the same [29]. By linking the respective elements accordingly, the generalized model takes into account the individual contribution of the relaxation time of each Maxwell element to the total stress relaxation [30]. The generalized Maxwell model can be expressed using the following equation:

$$\sigma(t) = \sum (G_i^* \varepsilon (t - \tau i)) \tag{2.8}$$

Here, G_i denotes the shear modulus of the elastic constituent of the i-th element in the model, while τ_i is the relaxation time of the i-th element. It is often very helpful to express this in the form of *Prony series*, which can be written as follows:

$$g_R(t) = 1 - \sum_{i=1}^{N} \bar{g}_i^P \left(1 - e^{-t/\tau_i^G}\right), \tag{2.9}$$

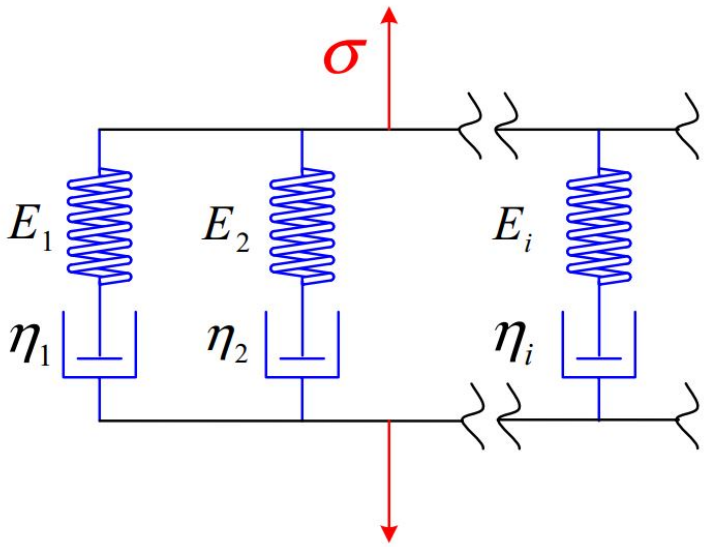

Figure 2.7: A schematic of the generalized Maxwell model, reproduced from[28].

where g_j in this equation denotes the non-dimensional shear modulus.
These expressions are commonly used for the direct definition of viscoelasticity in computational material simulations, such as finite element modelling, which will be discussed in the following section.

2.6 Finite element analysis

Finite element analysis is a commonly used computational tool for tackling problems that are very difficult to solve analytically. This involves dividing the structure into smaller elements and prescribing specific boundary conditions that represent the constraints and interactions within the system. By solving for the equilibrium of each individual element within the structure, FEA aims to arrive at a global solution of the model, which would otherwise be very complicated to compute. FEA can be especially beneficial in any study of mechanical behaviour if it is also backed up with experimental testing. [**gibson2021additive**]
Based on the introduction of all the necessary concepts, the finalised objectives of this thesis can be formulated.

Thesis objectives

- Design a FEM model applicable to the analysis of spinodal structures in compression in a viscoelastic regime.
- Perform an experimental stud based on dynamic mechanical analysis to validate material properties for the FEM simulation.
- Examine the patterns and differences in terms of reaction force in the compression of lamellar, columnar and cubic spinodoid structures.
- Analyse the dependencies of the mechanical response on the design parametrisation. Compare also the axis of compression.
- Develop a machine learning model in an attempt to validate the simulation results and predict the behaviour of structures with arbitrary design parameters.

3 Data pre-processing

3.1 STL generation

3.1.1 Code overview and parametrization

Before describing the specifics of the FEM model, we shall first introduce the course of topology generation. To begin with, the GIBBON toolbox was employed for processing the supplied spinodoid code, written by Kumar and Kochmann [5]. GIBBON (Geometry and Image-based Bioengineering add-On) is an open-source MATLAB toolbox, designed to aid with a variety of image operations, including meshing and image segmentation. In the context of this study, GIBBON was utilized for generating data on vertices and planes that constitute the spinodoid topology.
The provided spinodoid code offers a variety of tailorable parameters which can be adjusted when rendering the topology. These features are related to the underlying Gaussian random fields. As mentioned previously, the paper by Kumar et al., which serves as the foundation for this thesis, centres around the introduction of anisotropy to the GRF-based description of spinodal decomposition initially formulated by Cahn (Equation 2.2). The approach proposed in the paper involves narrowing down the range of values allowed for the n^{ith} direction vector, through the implementation of a non-uniform orientation distribution function (ODF) to introduce a bias in the statistical sampling, as opposed to simply sampling them isotropically from a unit sphere [5]. The distribution used in their work is as follows:

$$\boldsymbol{n}_i \sim \mathcal{U}\left(\left\{\boldsymbol{k} \in S^2 : (|\boldsymbol{k}\cdot\hat{\mathbf{e}}_1| > \cos\theta_1) \oplus (|\boldsymbol{k}\cdot\hat{\mathbf{e}}_2| > \cos\theta_2) \oplus (|\boldsymbol{k}\cdot\hat{\mathbf{e}}_3| > \cos\theta_3)\right\}\right) \tag{3.1}$$

The vectors stem from the Cartesian basis. The three angles, θ_1, θ_2 and θ_3 represent the allowed spread of wave vectors about each of the three orthogonal base directions, X, Y and Z respectively. Adjusting these angles allows for achieving a specific "type" of anisotropy. Four main types of structures can be highlighted. If θ_1 and θ_2 are set to zero, a cone is drawn within the unit sphere. The cone will span the angle determined by the value of θ_3, and all the allowed direction vectors will be contained within it. If the value of θ_3, in that case, is set to be $\pi/2$, the resulting equation will describe an isotropic system. However, as soon as the values of θ_3 start decreasing, an anisotropy is gradually introduced into the system, and a lamellar topology is generated. By introducing nonzero values of θ_2 and θ_1, one can arrive at 2 other "types" of anisotropy: columnar and cubic. Columnar anisotropy results from two θ parameters being set to non-zero values, while cubic structures emerge from all three θ parameters being non-zero.
Once the theta parameters are defined, the resulting phase field is used to build a "bicontinuous topology" based on the computation of isosurfaces (level sets). This data is all contained within the supplied GIBBON-compatible code, to which no alterations were made for the purpose of this project. It is still important to mention that there is a range of parameters within the code other than θ angles that can be adjusted. These parameters

result from the equation 2.2, and include: the number of waves contained in the GRF, the relative density of the resulting spinodoid topology (assuming one of the phases is solid) which can take a value from 0.3 to 1, the wave number. In practical terms, the wavenumber β is related to the "length scale" in the microstructure, i.e. how "fine" is the spinodoid. An additional parameter is also the resolution of the topology, which refers to the number of points sampled from the Gaussian field.

3.1.2 STL processing and volumetric mesh generation

An intermediate technical step in spinodoid generation involves additional structure smoothing using mex compilers before the STL file is exported for further processing. At this stage the quality of the triangular, surface mesh is still relatively poor, hence an intermediate processing step is necessary before the surface mesh can be converted into a volumetric mesh suitable for FEM. Multiple approaches for mesh conversion were tested, and the most successful involved using Autodesk Meshmixer, followed by Altair Hypermesh software. The details of mesh processing will be discussed in the following section. In principle, it is possible to perform the mesh conversion from the surface mesh into a volumetric mesh directly in the FEM software (in this case Abaqus), however, after multiple trials, it was found that especially for more complex structures the meshing algorithms embedded in the Hypermesh result in better quality mesh generation.
After the STL file was exported from Matlab, it was processed in Meshmixer software to perform initial mesh corrections using the 'Auto Repair All' inspector tool. In principle, the original spinodoid code included a directive to retain only the largest enclosed volume within the defined unit cell. Meshmixer software was used to validate this and remove any smaller volume elements ("floating pieces") that might have remained. In the following step, the mesh was loaded into Hypermesh software, scaled for convenience, and remeshed for improved mesh quality using the automatic meshing tool. It is important to highlight a few tailorable parameters in the remeshing process as well. The properties of the spinodoid mesh have a direct impact on the accuracy of the simulation, as well as on the time taken to run each simulation. These parameters include mainly the size of the elements contained within the mesh, their shape, order (i.e. the number of nodes), and the homogeneity of the mesh.

As previously mentioned, the meshing of the structures was done largely using the automatic meshing tool built into the HyperMesh software. However, a number of parameters guiding the meshing were user-determined. Among these, a key factor which needed to be specified was the target element size. This parameter was directly tied to the overall number of elements within the structure, thus influencing both the accuracy and efficiency of each simulation. The procedure for determining the element size, i.e. the mesh sensitivity analysis, is described in the following section (3.2). Hypermesh software offers also a large variability in meshing preferences for optimising the mesh quality according to the desired analysis purpose. For this study, a 2D mesh comprised of 3-node (1st order) triangular elements was built. Figure 3.1 displays the breakdown of the criteria for checking the quality of the individual elements. The criteria which were deemed to be the most relevant and used in the 2D-mesh generation are listed alongside the checked checkboxes. Once the improved 2D mesh was defined, the subsequent step involved generating a volumetric mesh using four-node (1st order) tetrahedral elements (C3D4). This choice was made because the mesh quality achieved was superior when compared to creating the mesh directly in Abaqus, and the generation also required less time. Once the

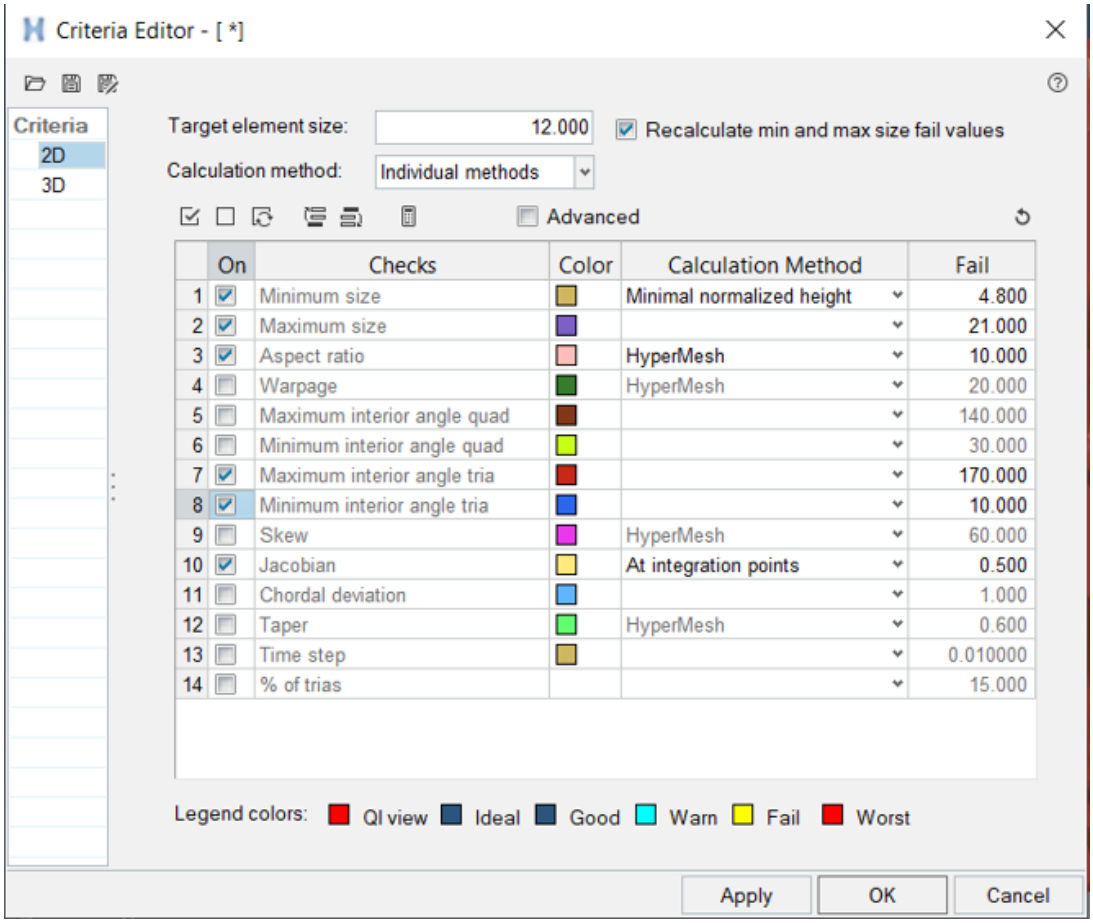

Figure 3.1: Criteria used for mesh generation in Altair Hypermesh.

solid mesh was created, all the triangular elements were removed leaving out only the tetragonal segments. The resulting structure was then exported as a .inp file, compatible with Abaqus software.

3.2 Model accuracy validation studies

3.2.1 Mesh sensitivity study

An important step in the model definition involves the mesh convergence study. Its main purpose is to determine the approximate number of elements necessary for obtaining accurate simulation, while the computation time is not compromised in consideration of the available hardware.
The usual approach to performing the mesh sensitivity analysis is to start with meshing the object using as few elements as reasonably possible, and then follow with gradually increasing the number of elements and comparing with the previous simulation until the

point of convergence. In this work, an initial mesh convergence study was performed on a smooth periodic isotropic spinodoid, with a wave number β of 3 and a resolution of 70. The topology was scaled up 14 times, to achieve a unit length of approximately 1000 in order to keep the unit consistency within the Altair software. Initially, the target element size was chosen to be 22 (around 360 000 elements), and then the number was gradually decreased until the average size of 10 (approx. 2 million elements) was reached. The structure was then assigned arbitrary hyperelastic material properties, and compressed to 0.4 of its length. Hyperelastic material model was chosen to initially test the mesh on an easy model, also potentially suitable for larger deformations; hence not linear elastic. The incompressibility of the structure was assumed. Figure 3.2 shows the result of this mesh sensitivity analysis. It can be seen that the overarching plot outline maintains a consistent

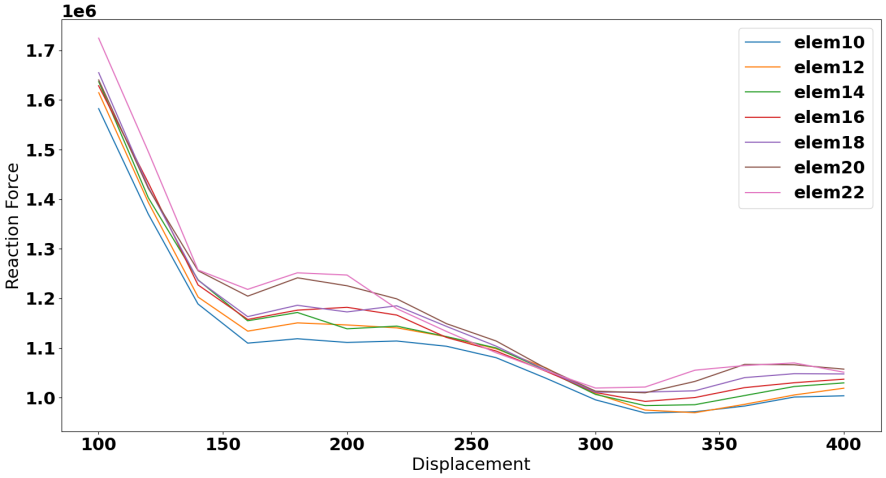

Figure 3.2: The initial performed mesh sensitivity analysis.

structure for all of the chosen element sizes. Notably, for element sizes 20 and 22 a slightly larger deviation is observed; hence a deliberate choice was made to retain sizes 18 and below for further analysis. Additionally, it was observed that choosing an average element size of 12 rendered the simulation acceptably efficient in computational terms, and its deviation from the average element number of 10 was deemed negligible. Therefore, for the subsequent meshing, an attempt was made to aim for an average element size larger than 12.

The mesh sensitivity test was redone in the later part of the study, in order to confirm the validity of the analysis once all the definitive simulation parameters were determined. The results of that validation are shown in Figure 3.3. As observed, although relatively minor, the discrepancy between the two simulations is still visible. Since simulations with elements of size 12 were still computationally affordable, a safety margin for accuracy was maintained by aiming for elements of approximately size 12.

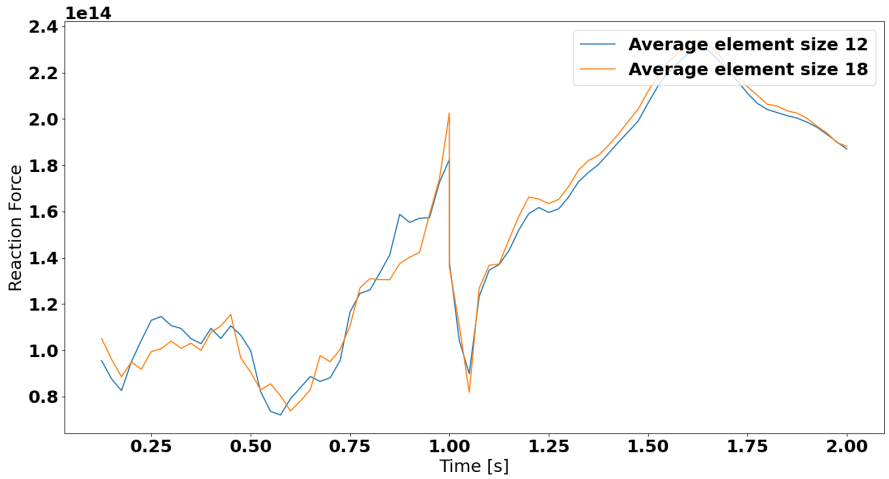

Figure 3.3: Repeated mesh sensitivity for the final model simulation.

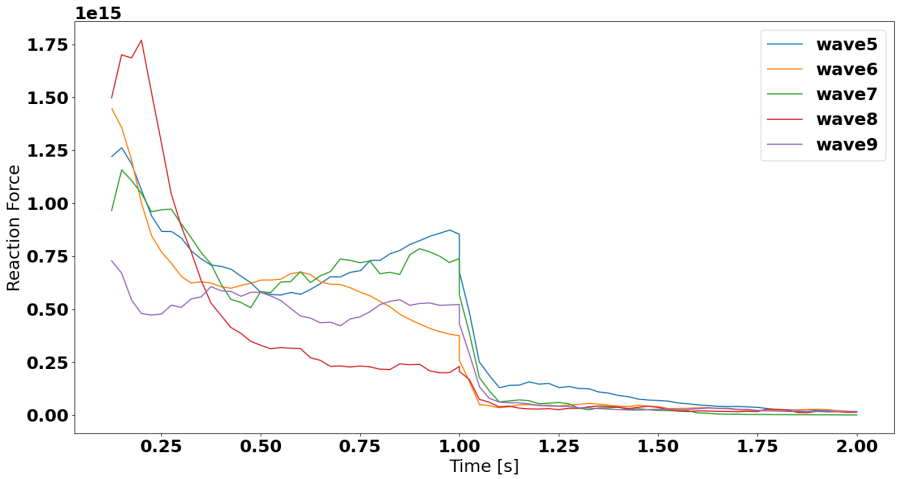

Figure 3.4: Wave number convergence for periodic lamellar structures.

3.2.2 Wave convergence study

After performing the mesh sensitivity analysis, another validation study was the wave convergence analysis. The purpose of this test was to find the smallest wave number value for which the compression test results convergence is observed. The wave number convergence study has been performed based on the work done by Soyarslan et al. Their research group worked on GRF structures generated using a specified wave number, with wave directions randomly distributed and contained within a spherical angle of 4 pi. [21]. In the initial part of their work, they focused on determining a material volume (referred to

as RVE) defined in terms of wave numbers, that is sufficient to statistically represent the general behaviour of a non-homogenous material. It is emphasized that the length scale should be greater in size in comparison to the microstructural features, and sufficiently below the macroscale lengths.
The researchers calculated the effective elastic moduli and Poisson's ratio for spinodal topologies using various wave numbers and two distinct volume fractions. They subsequently graphed these values against their corresponding volume element sizes and noted a convergence point at approximately 12 wavelengths. Initially, a wavenumber

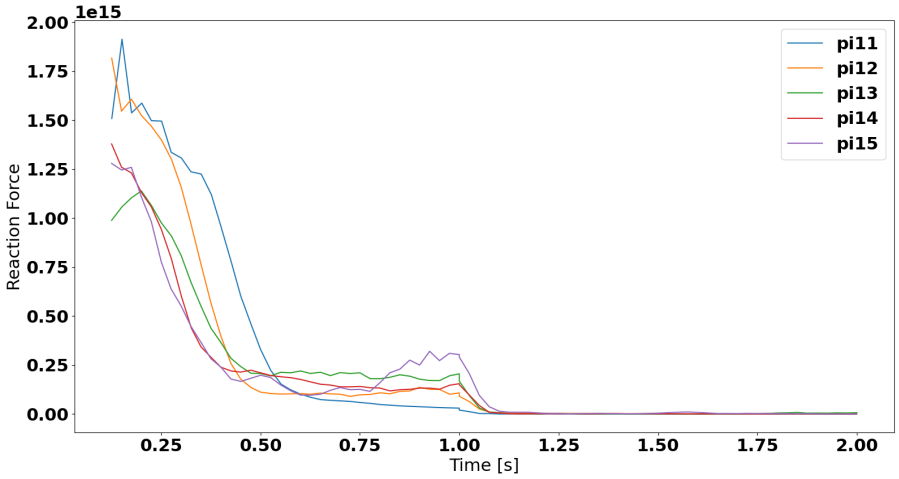

Figure 3.5: Wave number convergence for non-periodic lamellar structures.

convergence study was performed for the periodic spinodoid structures. Five periodic lamellar spinodoids with wave numbers ranging from 5 to 9, theta angle configuration of (0 20 0) and resolution of 100 were tested in compression along the Y axis, i.e. perpendicular to the lamellae. Initially, it was intended to include also topologies with higher wave numbers; however, meshing of these structures proved to be very challenging. The samples were tested following the previously determined protocol. The results of the test were shown in figure 3.4. As it can be concluded from the plots, the periodic structures, unfortunately, did not exhibit a satisfactory wave convergence for the chosen wave numbers. Therefore, a subsequent wave convergence study was attempted on the non-periodic structures.
The study on non-periodic spinodoids was run following exactly the same conditions as for the periodic structures. Corresponding wave numbers of Pi10 to Pi15 were analysed, and the results were plotted (Figure 3.5 Given that the non-periodic structures exhibited significantly better convergence behaviour, all subsequent investigations were focused on these structures.

4 FEM Simulation

In principle, when designing a finite element model simulation, both the pre-processing, as well as the post-processing, are crucial components. In a strictly theoretical sense, the initial requirements in a FEM model pre-processing stage include listing all the assumptions related to the set-up, and appropriate discretization of model constituents. The following steps involve an attempt to define an idealized material and elemental behaviour, and setting conditions defining the equilibrium for each of the elements in the model. Finally, the whole system needs to be assembled in such a way that the global equilibrium is ensured as well, after which all the boundary conditions and loads can be applied. The discretization of the model has already been discussed in the previous chapter. After spinodoid structures have

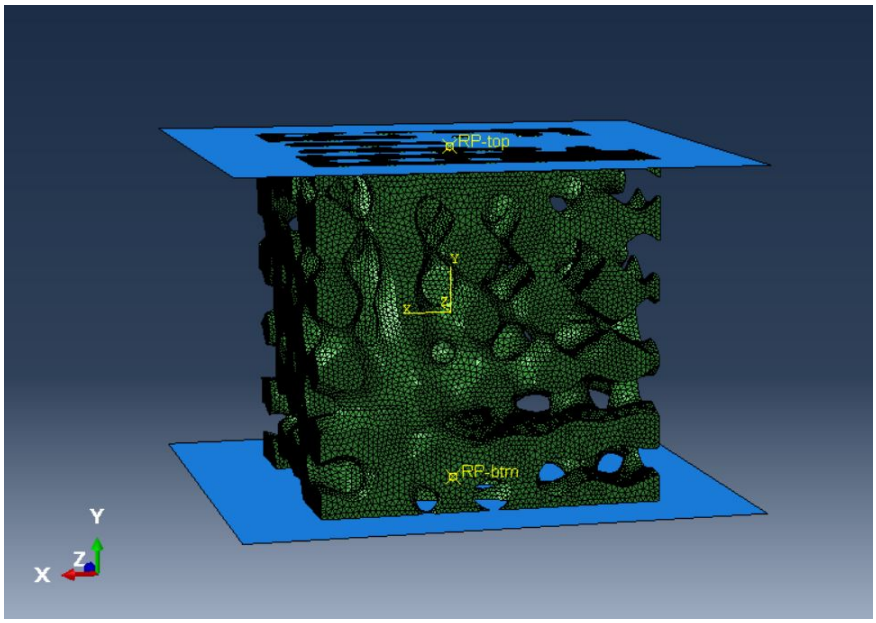

Figure 4.1: The schematic of compression assembly for a cubic spinodoid.

been generated and a volumetric mesh has been defined on each of the structures, the next step involved deciding upon specific simulation parameters. In this section, the reasoning for each selection will be presented. It has to be noted, that due to the sheer number of variables and tailorable settings in a FEM model design, the decisions made on the specific parameters will always be, to some extent, arbitrary, as the number of combinations possible is virtually infinite.

4.1 Model assembly

First, the spinodoid part was input into ABAQUS software, and its outer surface was defined. Then, two subsequent parts were created, which were to serve as the top and bottom planes in the compression test simulation. They were modelled as square-shaped, analytical rigid parts, and it was ensured that their unit length is about 1.5 times longer than the unit length of the modelled cube. Each rigid plane was also assigned a reference point (RP) since analytical rigid parts intrinsically do not contain geometry. The location of each RP was at the centre of the plane, overlaying the previously established datum point located midway between opposite diagonal corners of each plane. The assembly was then created by overlapping the reference point in the top and bottom rigid planes with the central point in the top and bottom sides of the spinodoid structure, as shown in figure 4.1.

4.2 Defining material parameters

After assembling the model, the selection of material properties and the viscoelastic model governing the deformation were considered. For the sake of simplicity, the decision was made to use the generalized Maxwell model explained in an earlier chapter. Additionally, it was decided to exclude any volume changes in the material from consideration.
In principle, if a mechanical test is performed, i.e. there is an experimental creep or stress relaxation test data available, it can be input into Abaqus software directly and computed into the Prony series directly in the software. Initially, it was intended to conduct mechanical testing to determine the material properties for the simulation; however, because the mechanical testing attempt yielded unsuccessful results (as elaborated in chapter 5), using literature data was chosen as an alternative solution.
In the absence of available mechanical testing data, the viscoelastic Prony series parameters can be used directly in the model definition. The specific parameters required by FEM software may vary; Abaqus in particular requires the specification of material in terms of three parameters: g_i, k_i and τ_i. The first parameter, g_i refers to the shear, k_i is linked to the volumetric behaviour, and τ_i represents the relaxation times. For this model, k_i was hence set to zero, based on the previous assumption that volumetric variations in the material are negligible. Prony series in Abaqus can be defined in either the time or the frequency domain. Time-domain viscoelasticity is related to the study of creep and stress relaxation; while the analysis for frequency domain is appropriate for simulations based on sinusoidal excitation; and it is only permitted in Abaqus standard, i.e. the implicit solver. Therefore, the Prony series parameters were defined in the time domain. Guided by the main premise of the work, the aspiration was to search for parameters defining the viscoelastic behaviour of one of the common polymeric biomaterials used in bone scaffold or implant manufacturing. While exploring potential solutions, consideration was given to commercial material databases. One such database, polyUMod, provided commercial mechanical testing data for polyether ketone (PEEK) tested at various strain rates. PEEK has been previously documented as a biomaterial used for bone regeneration purposes, and it has the advantage of high stiffness, allowing for it to be used in load-bearing applications. Nevertheless, finding or computing Prony equation parameters remained challenging. The parameters related to viscoelasticity provided by the manufacturers or in material databases tend to vary largely, even for the most common materials. This is due to a

multitude of variables that have a direct effect on the testing results, which include the material's specific crystallinity, its blend composition (for example, the stiffness of polystyrene-polyisobutylene-polystyrene would be different from that of pure polystyrene), any variations in temperature during testing, or even the algorithms used for data conversion, among others. What is more, it was found that the studies on PEEK usage as bone biomaterials were focused primarily on incorporating it as a constituent in composites. This led to questioning whether the material would still be appropriate to model viscoelasticity.

4.2.1 Cortical bone properties

Bone Type	Density (kg/m^3)	Elastic Modulus (GPa)	Tensile Strength (MPa)	Compressive Strength (MPa)	Ultimate Elongation (%)	Ultimate Contraction (%)
Cortical	1700–2000	5–35[a]	55–200[a]	106–224[a]	0.5–4.9[a]	1.7–2.7[a]
Cancellous	100–1000	0.001–98	0.9–5.4	0.1–310	0.9–3.5	1.1–13.4

[a] In the direction of the long bone axis.

Figure 4.2: Physical and material properties of human cortical and cancellous bone, reproduced from [31]

Further exploration of the available material databases led to the idea of using material parameters intrinsic to human bone, rather than a synthetic biomaterial. The initial simulation was run using the generalized Maxwell model parameters. The values taken were based on the paper by Brewick et al. [32], which were displayed in figure 4.3 The reasoning behind this decision was that since the principal aim of the study is to investigate the structure-property relationship in various spinodoid topologies, the choice of the simulation material becomes somewhat arbitrary. However, as the starting point for these deliberations was the potential application of spinodoid architectures in regenerative medicine and specifically bone tissue engineering, it seemed justifiable to use parameters describing the viscoelasticity of bone tissue. For convenience (to speed up the simulation, to be precise) it was decided to use specifically the parameters obtained for cortical bone, as it has a higher Young's modulus - the paper cites 16.77 GPa and 533 MPa for cortical and cancellous bone respectively (which is in agreement with the table presented in figure 4.2. Another argument for disregarding the cancellous bone in this simulation was that spongy bone is a naturally porous structure. While cortical bone itself is not a perfectly dense tissue either, it is easier to consider it as a viable material to be used as a bulk material parameter, particularly for metamaterial considerations. Additionally, the elastic modulus of the material is one of the parameters that impact the simulation running time. Hence, with this added incentive, the analysis in this part focuses solely on using cortical bone as a base material. In addition to these properties, the material was assigned the average density of the cortical skull bone, 1841 kg/m3. It was also defined to have a Poisson's ratio of 0.3 [32].

Table 4: Parameter Values for the Viscoelatic Model of Cortical Bone

Prony Series Model		g_j	τ_j	$\overline{O}$
2-term model	$j=1$	0.4838	1.32×10^{-5}	0.4124
	$j=2$	0.1336	6.00×10^{-2}	
6-term model	$j=1$	0.0186	8.73×10^{-1}	0.3858
	$j=2$	0.0175	8.73×10^{-1}	
	$j=3$	0.0180	8.78×10^{-1}	
	$j=4$	0.0176	8.75×10^{-1}	
	$j=5$	0.0792	1.56×10^{-2}	
	$j=6$	0.4772	1.29×10^{-5}	

Figure 4.3: Prony series parameters for cortical bone tissue, adapted from [32]

.

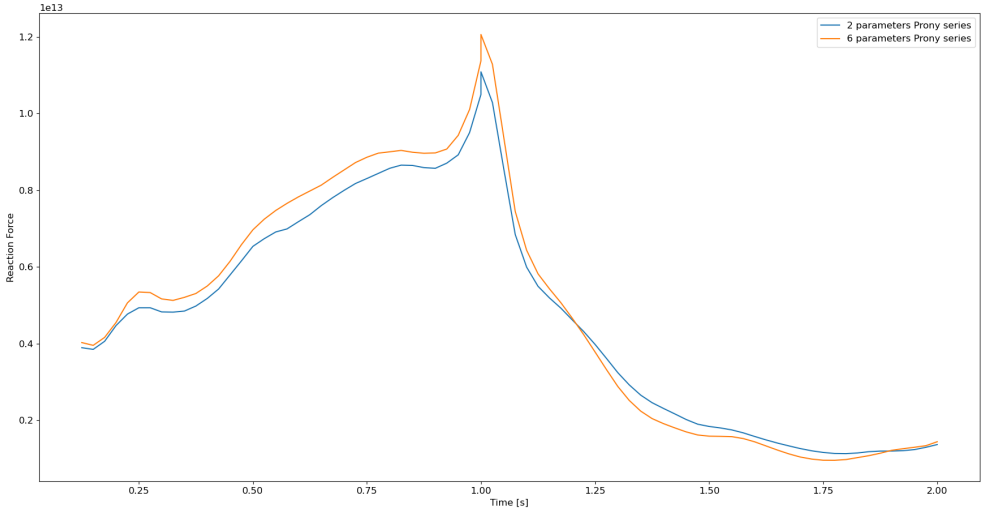

Figure 4.4: An arbitrary simulation result for a spinodoid with viscoelastic material properties defined by a Prony series adapted from [32], with 2 and 6 parameters.

.

4.3 Solver choice

Abaqus software offers two main types of solvers: Abaqus standard, which is the implicit solver, and Abaqus explicit. Implicit solver is primarily considered for simulations that aim to solve for static equilibrium conditions, while explicit solvers are commonly utilised in dynamic models, for example, when the user wants to study high-impact phenomena. After longer consideration, a dynamic explicit solver was chosen for the analysis due to the efficiency of the simulation, as well as the advantage in surface interaction definition compared with the implicit solver.
The surface interaction for this simulation was hence established in the first step, and defined

as general contact (explicit). The contact domain included all the defined surfaces, that is the outer spinodoid surface and the surfaces in the top and bottom planes which were in contact with the structure, as well as self-contact for all the surfaces, to prevent any self-penetration in cases where different regions of outer spinodoid surface would touch. The interaction properties were set to include tangential behaviour, isotropic friction, with a friction coefficient of 0.6, and normal "hard" contact behaviour. The second interaction property implies contact pressure transmission when the surfaces are touching.

4.4 Loading definition

4.4.1 Steps and frames

As previously outlined, the loading pattern was defined to be 1 second of uniaxial compression, followed by one second of holding (Figure 4.5). The active simulation was

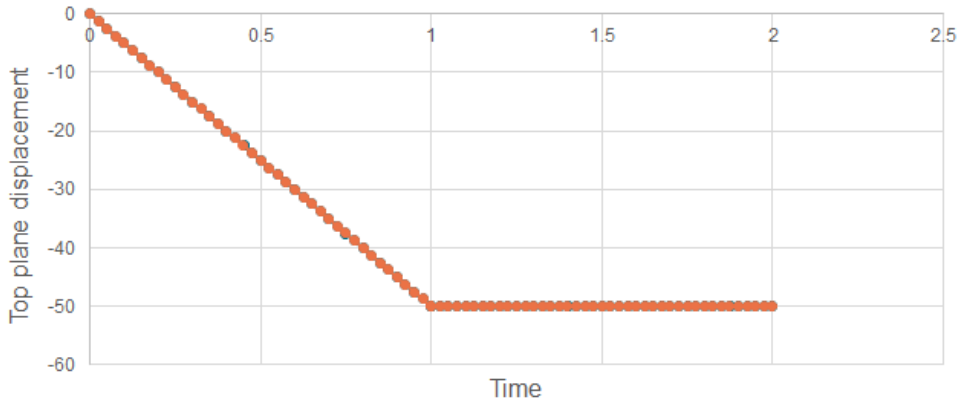

Figure 4.5: The displacement of the top plane in time.

therefore split into two steps (excluding the initial, default step). The first step involved the movement of the top plane. Its duration was set to the default 1 second, and the number of frames within the step was doubled. It is important to note that a larger number of frames leads to an extended simulation duration, whereas fewer frames can potentially yield the simulation less accurate, and results in fewer recorded data points. Therefore, the number of frames was nominally increased to 40 instead of the default 20. Afterwards, the second step was created in order to record the behaviour of the structure during holding. During this step, the top plane was immobilised.

4.4.2 Amplitude definition

Explicit solver in Abaqus does require a defined loading amplitude. In this simulation, a default tabular amplitude was used, defined as shown in figure 4.6.

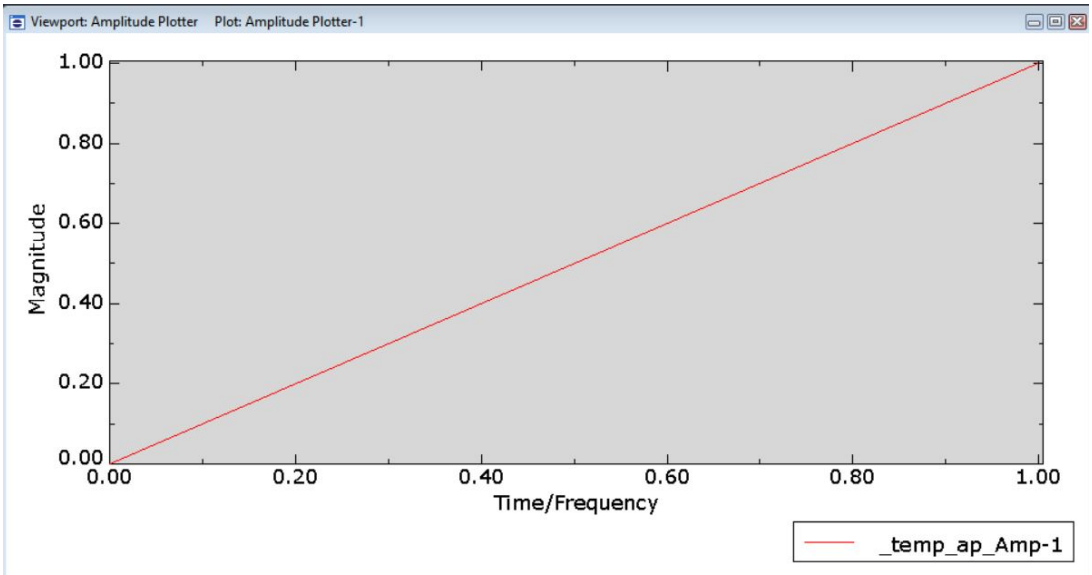

Figure 4.6: Tabular amplitude definition.

4.5 Mass scaling

Although the material properties chosen were based on a human bone, for the consideration of the computational time the decision was made to introduce a mass scaling factor, which artificially increases the density of the material. The impact of mass scaling on the simulation times has been significant. Figure 4.7 shows the mass scaling parameters and the corresponding recorded simulation times (for reference, the automatically fitted equation for generating the trendline was $y = 151.35x^{-0.492}$). Additionally, mass scaling was introduced due to a relatively long analysis duration, i.e. 2 seconds, compared to conventional simulations run in the explicit solver. For validation purposes, a single simulation was run to compare the results obtained with mass scaling to the model with a higher intrinsic density. Figure 4.8 shows the recorded reaction force for compression of a structure scaled with a factor of 100, compared to the same structure with no mass scaling and density increased by a factor of 100.

4.6 Constraints and boundary conditions

The first boundary condition was created in the initial analysis step and propagated in the subsequent steps. By applying an 'encastre' command on the bottom plane's reference point, it was ensured that any translational or rotational movement of the plane was constrained in all three possible directions. The second boundary condition was applied to the reference point in the top plane. For the compression tests performed along the Y axis, top plane RP was constrained in the X and Z directions, and mobile in the Y direction. Any rotational movement of the top plane RP was suppressed. Analogous constraints were applied for compression along the X-axis. The third BC was also applied on the top plane reference point in the subsequent analysis step, prescribing a displacement of -50 units in the Y direction.

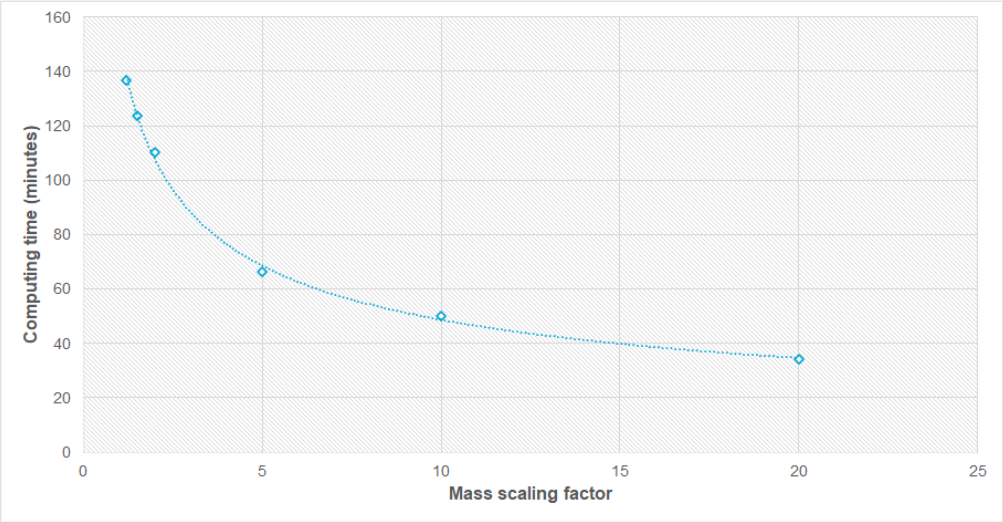

Figure 4.7: The variation of computation time with respect to the mass scaling factor applied.

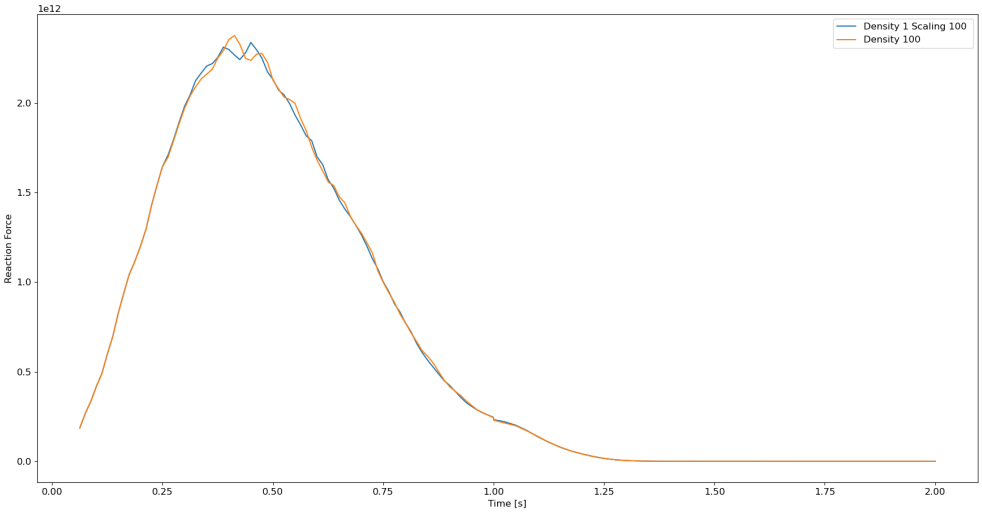

Figure 4.8: Comparison of the results obtained for a structure with 100-fold mass scaling and a structure with 100 times larger density and no mass scaling.

The compression distance was chosen based on the data from the literature on the stresses and strains that human bone tend to be exposed to. As highlighted in the table **??**, the ultimate percentage elongation of a cortical bone reaches almost 5%; hence the value for compression was chosen to be 5%.

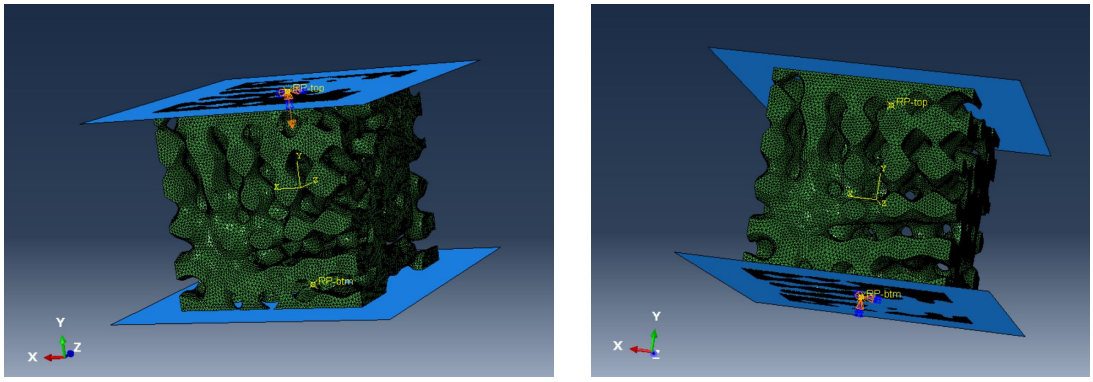

Figure 4.9: Visual representation of the applied boundary conditions.

5 Experimental contribution

The initial objectives of this work involved, alongside the simulation work, also an experimental contribution. The aim was to use an additive manufacturing method to fabricate test samples, which could then be used for determining the mechanical properties of a viscoelastic material. The ultimate goal of the experiment was to perform a DMA analysis on a range of spinodoid samples and investigate how the θ parameters influence the test results. The first stage of the testing involved 3D printing dog-bone samples with varied printing orientations, i.e. at 0, 45 and 90 degrees with respect to the symmetry axis of the specimen. The purpose of this study was to test these samples in an Instron. The objective was to investigate how the samples behave when they undergo cyclic loading and loading with varied strain rates; and based on the observed behaviour determine the Prony series parameters of a chosen constitutive viscoelastic model, which could be used in the FEM simulation. In ideal conditions, provided the availability of the appropriate facilities and materials, the goal would be to use a polymer conventionally used for manufacturing bone. However, due to the limitation in the accessibility of such materials and printing facilities, as well as the time constraints of this thesis, another available polymeric material was used. This is still in line with the main objective of this work, as the overarching goal is to examine the general behaviour of spinodal-like structures in the viscoelastic regime, without limiting the material properties to any specific materials. It is worth noting that, in an ideal scenario, a self-assembly process would be used in spinodoid manufacturing. However, up to date, the conventional approach to fabricating topologies with that level of complexity and intrinsic detail is through various additive manufacturing techniques. The general premise of AM technology was already introduced in the previous chapter, in this section only two specific techniques, stereolithography (SLA) and fused deposition modelling (FDM), will be outlined, as these were the two types of 3D printers available on TU Delft campus.

5.1 SLA

Stereolithography, often abbreviated as SLA, is a vat photopolymerization technique which can be used to process UV-curable polymers. This technique is based on selective curing of a liquid polymer resin in a layer-by-layer manner. Digital light projection (DLP) is a variation of that process, which uses a projector as a light source instead of a laser. This generally leads to a voxel formation along Z-axis in the structures produced by DLP. SLA and DLP both allow to obtain relatively good mechanical properties, and their main advantage is the manufacturing precision, with features down to a few um achievable. However, the manufacturing process is rather slow, even when using a digital light source, and not easily scalable. Furthermore, the available materials are limited mostly to photosensitive thermosets (and potentially also the addition of ceramic monomers). [6]
The SLA printing method initially appeared to be a viable technique for manufacturing spinodoid test samples, primarily due to its capacity for intricate detailing and reduced

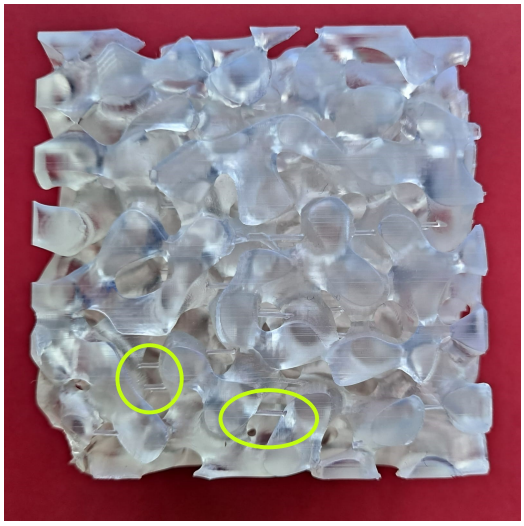

(a) An SLA sample, green circles highlight two examples of internal support structures within the topology.

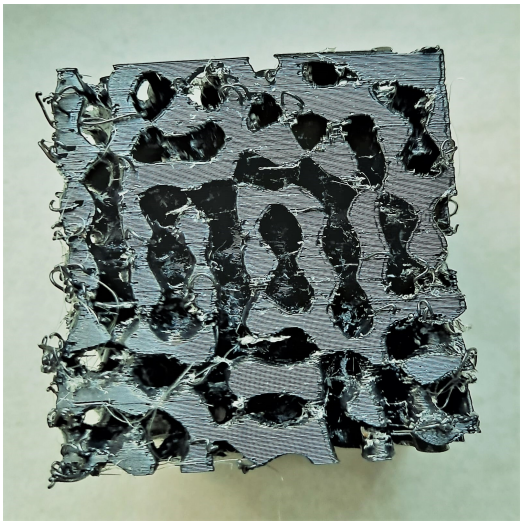

(b) A FDM sample.

Figure 5.1: Unsuccessful attempts at 3D printing spinodoid topologies.

susceptibility to inter-layer adhesion issues commonly encountered in FDM printing. Initially, the SLA printer was used to fabricate the dog bone samples, which were subsequently used for initial mechanical tests, the details of which are described in the following section. Unfortunately, SLA proved to be unsuitable for printing of the spinodal structures. This was due to intrinsic nature of the SLA process, where the same material, contained in a vat, is used for both printing and support structures. Consequently, vertical support columns were incorporated in the structure, as it was crucial to support the more intricate, internal features during fabrication. Consequently, these columns were rendered inseparable from the main component. Attempts were made to mitigate this issue by reducing the support material's thickness and exploring mechanical removal options, but that proved to be practically impossible due to the scale and the location of the features. As a result, this project, unfortunately, had to be abandoned. Figure **??** shows a photo of one of the SLA-printed spinodoids; with the support columns highlighted.

5.2 FDM

Following the unsuccessful SLA fabrication, an attempt was made to produce spinodoid structures using the Fused Deposition Modeling (FDM) technique. FDM is an additive manufacturing route in which thermoplastics are used as a build material. During the procedure, the material is first heated, deposited and cooled to achieve solidification and bonding between the subsequent layers. The achievable resolution and volume parameters typically range around 200-500 µm and several cm3, respectively.
FDM is one of the most inexpensive and readily accessible additive manufacturing methods; nevertheless, it is linked with certain limitations. These include relatively low resolution, heightened sensitivity to imperfections, and a pronounced effect of anisotropy with respect to the deposition direction, among others. A notable advantage of FDM is,

however, that, contrary to stereolithography, it allows for the utilization of dissolvable support materials, thereby affording greater freedom in creating complex internal structures.For that reason, a subsequent attempt was made to use FDM printers available at TU Delft facilities to manufacture spinodoid samples. Unfortunately, despite solving the issue with the support material, FDM also proved to be unsuitable for spinodoid manufacturing. The reason for that was the accuracy and the resolution of the prints being of very low quality; to the point that it would likely yield inaccurate results had the samples been tested in a DMA machine. Figure **??** displays the photo of one of the FDM-printed samples, with the imperfections clearly visible. In light of these failures, the attempt to include experimental work was, unfortunately, abandoned.

6 Data analysis

6.1 Final dataset overview

After conducting preliminary testing, a final set of topologies to analyse was determined, comprising lamellar, columnar, and cubic structures. It consisted of 6 lamellar, 36 columnar and 36 cubic spinodoids. Lamellar structures were defined by angles $\theta_x = 0$, $\theta_z = 0$, and θ_y taking a value of $t \times 10$, where $2 \leq t \leq 7$. Columnar structures were generated with the following angles: $\theta_z = 0$, $\theta_x = s \times 10$, and $\theta_y = s \times 10$, where $2 \leq s \leq 7$. Finally, for cubic structures, θ_z was set to always be equal to θ_y, while θ_x and θ_y were varied in the same way as in the columnar structures. The limitation of the number of cubic structures was done on purpose, as due to the lengthy meshing procedure, each added topology increased the time needed to acquire data.
The decision was made to use evenly distributed theta angle values for the ease of structure tracking and subsequent data analysis; however random angle sampling could be explored in future studies. Due to the limitations in pixel resolution linked to granularity, the generation of spinodoids with angles [60 60 60] and [60 70 70] yielded identical structures. This has been confirmed by examining the FFT projections of these structures, as shown in figure 6.1. Similarly, commands for rendering cubic spinodoids with angles [70 60 60] and [70 70 70] also returned the same structures. Therefore, in order to keep the previously established convention, the two repeated structures were excluded from the analysis. This yielded a total of 34 cubic structures modelled.

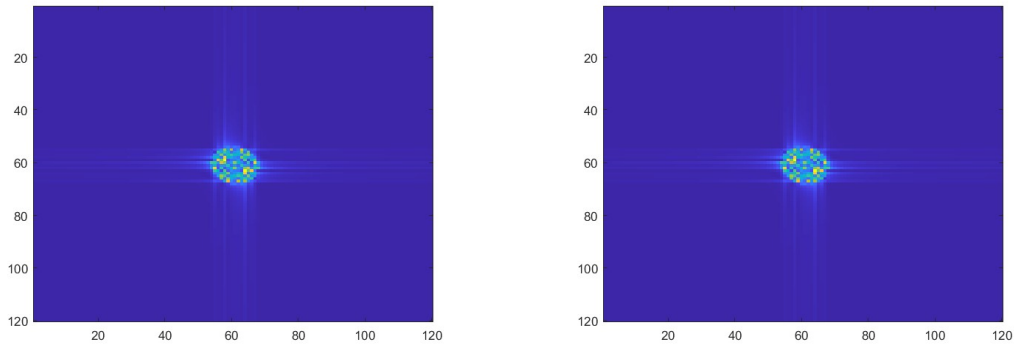

Figure 6.1: FFT visualisations generated for cubic [60 60 60] and cubic [60 70 70] topologies.

In the simulation set, each lamellar and columnar structure was compressed along the Y and X axis, and each cubic structure was compressed along the Y axis only. It is crucial to note here that the axis definition in Abaqus differs from the axis definition proposed by Kumar et al. Abaqus by default uses the Y-axis as the vertical axis, which in spinodoid's θ angle definition corresponds to Z-axis. In general, from this point on in the work, the Y and

X axis will refer to the direction defined in Abaqus unless otherwise specified.
Another important clarification is necessary regarding the theta indexing - for convenience, θ_x and θ_1, θ_y and θ_2, and θ_z and θ_3 are used interchangeably.

6.1.1 Post-processing steps

The general method used for the analysis was the plotting of the reaction force versus time. Since the displacement of the top plane was kept constant for all the simulations, plotting the force directly against time was feasible. Once all the simulations were completed, reaction force versus time data was exported from Abaqus software and processed using Python libraries. Prior to the data visualisation, a few post-processing steps were performed on each data set. Each dataset contained 82 points, 41 for each simulation step. The first step was the removal of the first two points from each dataset. These first two points represented the contact initiation between the spinodoid structure and the top plane, and often had disproportionately high values, leading to misleading conclusions. They were also likely influenced by the exact area of the spinodoid topology that was in contact with the rigid plane, and it was observed that they would differ significantly even when the same structure was analysed and compressed along the same axis, from either the top or bottom.
The next step of the post-processing was taking the absolute values of all the reaction forces recorded; since the compression was performed from positive to negative values the forces recorded also had negative values. This was done merely for the simplification of the visual analysis. The subsequent step involved data smoothing, using the 3-point-rolling average method. This was done to improve the quality of the data. A general Python code was compiled to perform these analysis steps on all datasets, once they were exported from ABAQUS.

6.1.2 Data analysis strategy

Naturally, it was rather difficult with the abundance of data to compare every plot in every combination. Hence, in an attempt to navigate the data analysis more effectively, a decision was made to follow a specific plan for the data analysis. The analysis started by examining the effect of theta variations within the same type of anisotropy. The initial step involved a visual analysis. To allow for visual comparison, data points generated for distinct structures were graphed within the same coordinate space. The procedure involved plotting a set of graphs sequentially, first by plotting structures with identical θ_1 values, followed by identical θ_2 values (provided they were not equal to zero). As a result, five subcategories of plots were created:

A. All lamellar structures compressed along the Y-axis – 1 plot.

B. All lamellar structures compressed along the X-axis – 1 plot.

C. Columnar structures compressed along the Y-axis:

- 6 plots comparing structures with equal θ_1 and varying θ_2.
- 6 plots comparing structures with equal θ_2 and varying θ_1.
- 1 plot comparing structures with $\theta_1 = \theta_2$.

D. Columnar structures compressed along the X-axis:
   - 6 plots comparing structures with equal θ_1 and varying θ_2.
   - 6 plots comparing structures with equal θ_2 and varying θ_1.
   - 1 plot comparing structures with $\theta_1 = \theta_2$.

E. Cubic structures compressed along the Y-axis:
   - 6 plots comparing structures with equal θ_1 and varying θ_2.
   - 6 plots comparing structures with equal θ_2 and θ_3, and varying θ_1.
   - 1 plot comparing structures with $\theta_1 = \theta_2 = \theta_3$

In total, 41 plots were generated to try to systematically examine the effect of θ parameter variations within individual anisotropic structural types. The details of that analysis will be discussed in the following section.
After acquiring data related to individual structures, the subsequent step involved comparing reaction forces experienced by different spinodoid types. Again, this analysis was also divided into multiple stages:

1. Comparison of reaction forces for selected lamellar structures under X-axis versus Y-axis compression.
2. Comparison of reaction forces for selected columnar structures under X-axis versus Y-axis compression.
3. Comparison of reaction forces for selected lamellar, columnar and cubic structures under Y-axis compression.
4. A Comparison of reaction forces for selected lamellar, columnar and cubic structures under Y-axis compression, as well as the lamellar and columnar structures under X-axis compression.

In the latter part of the analysis, a Python script was used to compute absorption energy for each structure. The final step involved the construction of a machine learning algorithm to try to predict the reaction force data.

6.2 Visual analysis of reaction force graphs

6.2.1 Lamellar structures

As described before, 6 distinct lamellar structures were generated and meshed. Each of them was compressed along the Y and X axis, as shown in figure 6.2. Figures 6.3 and figure 6.4 show the generated reaction force response in time for each of the two compression modes accordingly. As it can be observed, out of all 6 lamellar structures, spinodoid with [0 20 0] configuration has the lowest initial stiffness when compressed parallel to its lamellae (along the Y-axis), yet it is the stiffest structure when compressed along the perpendicular axis. Overall, the pattern that emerges from the analysis is that the structures which have smaller θ angles tend to exhibit higher stiffness, on average, in X-axis compression, while the opposite is true for the compression parallel to the lamellae. There is also a clear difference between the two compression modes in terms of how the stiffness response changes during

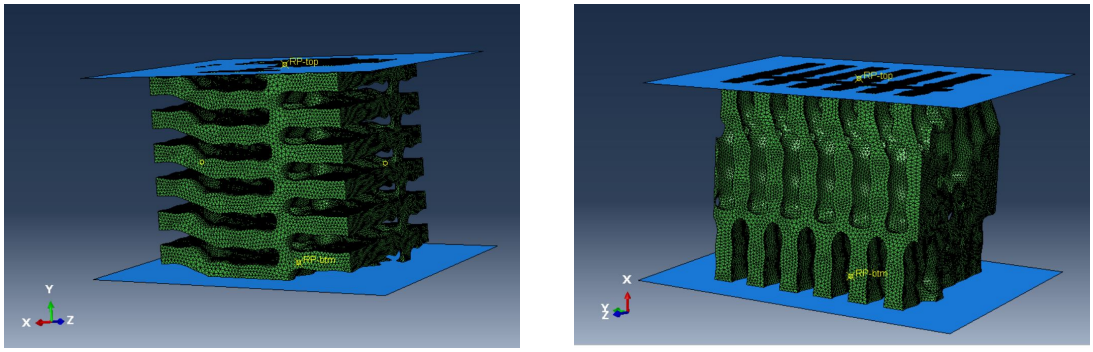

Figure 6.2: Simulation set-up for lamellar compression along the Y and X axis, accordingly.

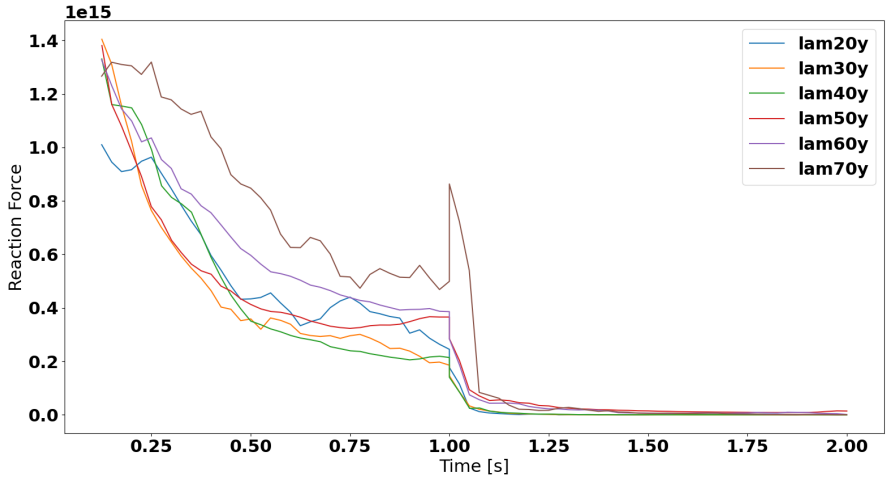

Figure 6.3: Recorded reaction force for 6 lamellar structures compressed along the Y-axis.

the loading step. In the Y-axis loading the decrease in stiffness ensues more rapidly, while for X-axis loading the stiffness decreases to a lesser extent, and only in the initial part of the loading, remaining approximately constant until the loading conditions change in the second step of the simulation. Additionally, the transition from the first to the second analysis steps occurs more smoothly for lamellar structures compressed along the Y-axis. In X-axis compression, on the other hand, the drop in reaction force values as soon as the top plane is immobilised is almost instantaneous. Subsequently, the data for selected structures, i.e. lamellar [0 30 0] and lamellar [0 70 0], was plotted together to compare the behaviour in different compression modes, as shown in the figure 6.5. While studying this combined graph the differences in terms of relative stiffness responses between the two compression modes. The differences in the stiffness behaviour throughout the first analysis step can also be observed more clearly, although in the case of lamellar [0 30 0] structure they are not as pronounced. Another prominent feature which stands out when analysing the plots is the sharp increase in the reaction force related to the transition between the loading steps. From the initial observation, one might deduce that these peaks are generally observed

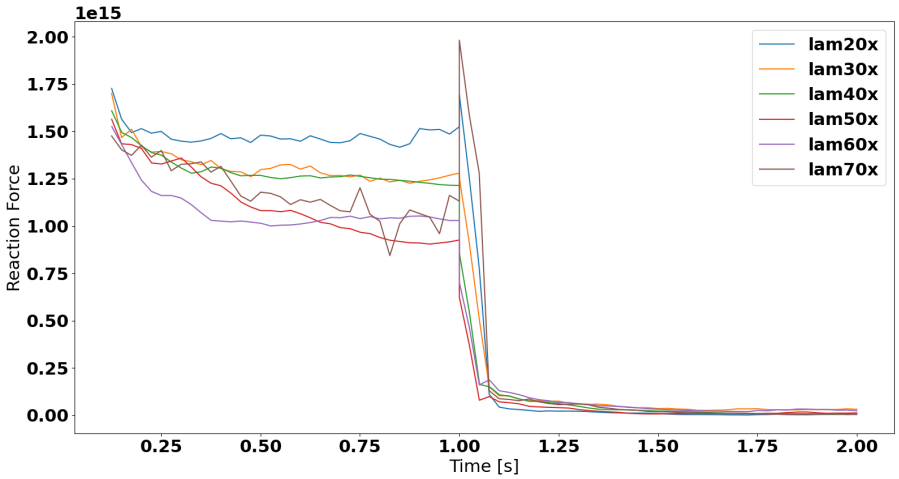

Figure 6.4: Recorded reaction force for 6 lamellar structures compressed along the X-axis.

independently of the loading mode, as observed, for example, for lamellar [0 70 0] topology. One has to also note that the response of [0 70 0] structure deviates rather strongly from the behaviour of other modelled structures in terms of the general response. Hypothetically, one of the reasons for this discrepancy, and a resulting 'outlier' behaviour could be a meshing error.

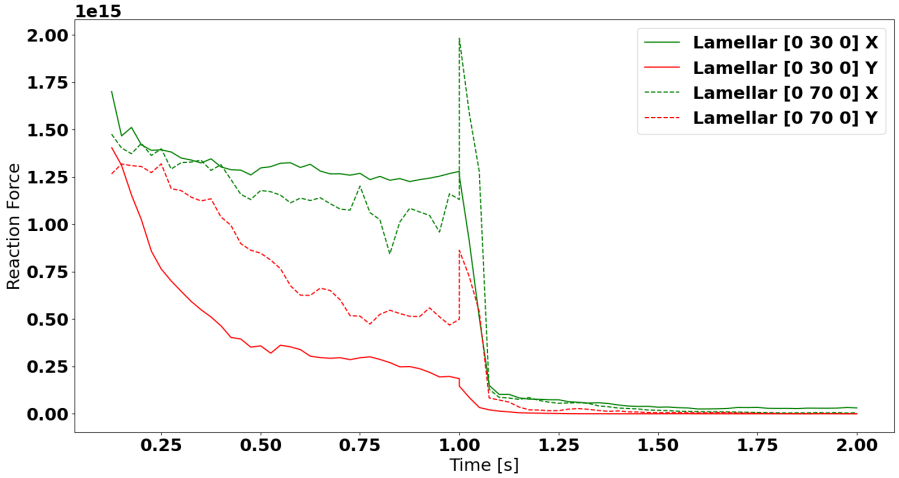

Figure 6.5: Recorded reaction force for selected lamellar structures compressed along the Y-axis versus X-axis compression.

6.2.2 Columnar structures

The simulation of columnar structures was executed following the same procedure as that of the lamellar topologies, i.e. 36 distinct columnar structures were generated and meshed and each of them was compressed along the Y and X axis. Due to the length constraints of this work, the main part of the report will not include all the plots generated for the columnar structures, and only the example plots, which are the most relevant for the analysis.
Purely from a visual inspection, the structures seem to follow a closer to an arbitrary stiffness response. The effect of the variation in the θ parameter is much less obvious than it is for lamellar structures. Overall, even without studying the plots, it can be deduced that the compression of the structures along the X-axis and along the Y-axis would yield different results. In this configuration, **when the structures are compressed along the Y-axis, the columns are aligned horizontally with respect to the loading direction**, i.e. they are perpendicular to the loading direction (akin to the lamellar alignment when compressed in Y-axis). Analogically, **when the columnar structures are compressed along the X-axis, the columns are oriented vertically,** parallel to the compression direction. These orientations are shown in figure 6.6. It is acknowledged that the notation can be confusing to the reader, mainly due to the shift in the axis labelling between the original spinodoid Matlab code and the axis definition in Abaqus software and hypermesh. The observation has been duly noted with the intention of improving the notation in any further studies. One can expect that there will be a difference in terms of the more

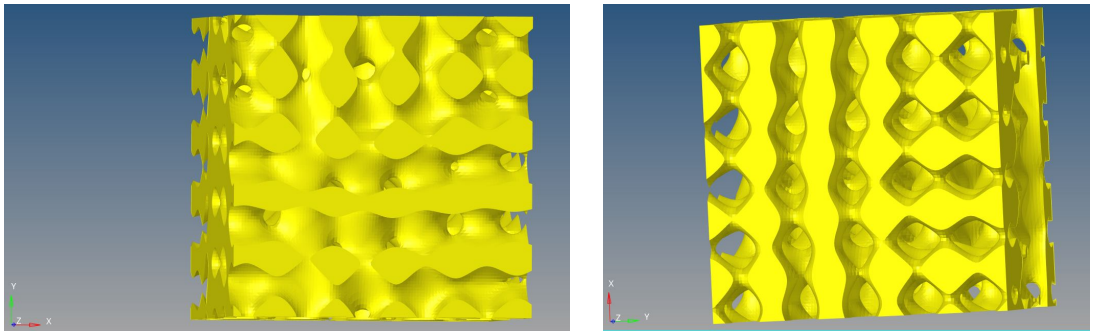

(a) Columnar orientation in the case of Y-axis compression.

(b) Columnar orientation in the case of X-axis compression.

Figure 6.6: Comparison of vertical and horizontal column orientations in different compression modes.

"influential" θ parameter for each compression mode, i.e. Y-axis compression is expected to be more affected by the variation in the θ_2 angle, while the X-axis compression would be stronger influenced by θ_1. This can be observed, for example, in figure 6.7, where for structures with θ_2 angle set to 70 there is a great similarity in the mechanical response of the structures for all angles θ_1 tested. Nevertheless, for this particular dataset drawing definite conclusions based purely on the visual analysis is very challenging. In such cases, the analysis of another parameter such as energy absorption, can prove to be helpful, as it will be discussed in the following section.
Another point worth noting is that, similarly to the lamellar structures, in the analysis of the columnar topologies data one can also pinpoint 'outlier' structures. Their response deviates rather significantly from the other structures. These structures have configurations [60 60 0], [20 20 0] and [40 60 0]. This effect is especially pronounced in figure 6.8, which is

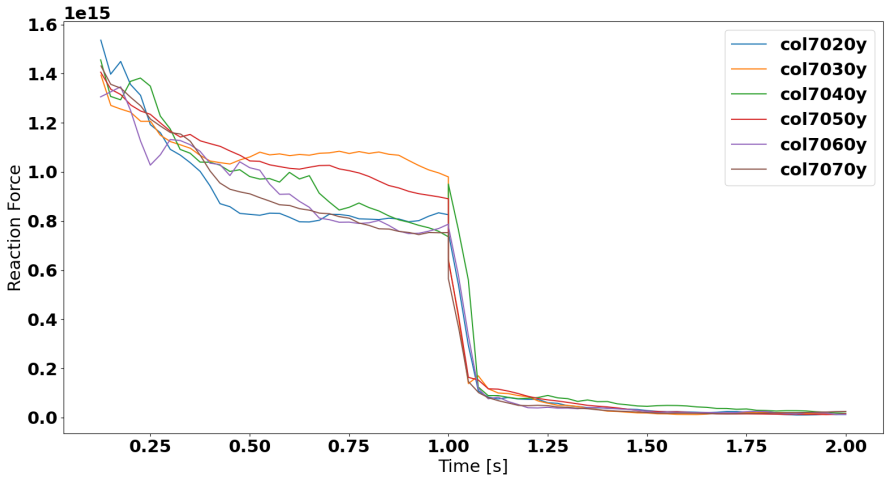

Figure 6.7: Reaction force recorded for columnar structures with θ_1 set to 70.

very unfortunate, as it significantly affects the quality of the analysis that can be performed on this graph. As mentioned before, compressing a structure along the X-axis versus

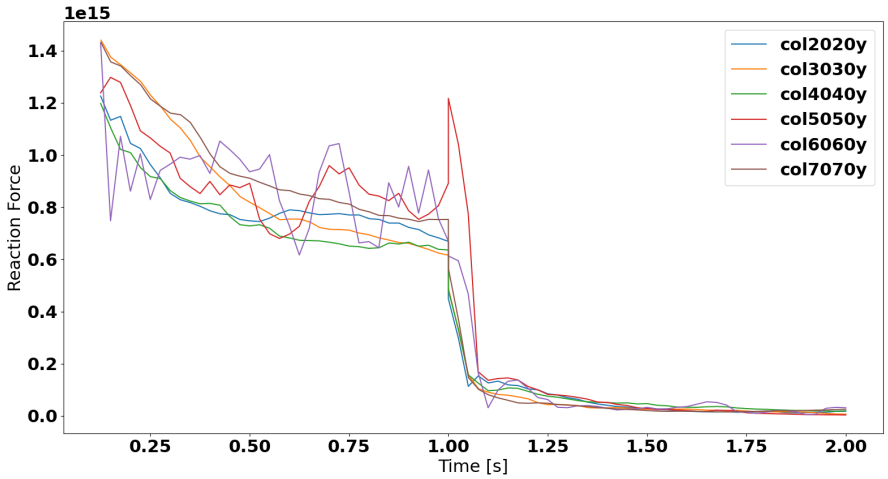

Figure 6.8: Comparison of reaction force response in Y-axis loading for columnar structures in which θ_1 is equal to θ_2.

compressing it along the Y-axis will likely produce different outcomes. Figure 6.9 demonstrates this difference in the example of two columnar topologies, [30 30 0] and [70 70 0]. As one might have expected, the configuration when the columns are aligned horizontally to the loading axis, i.e. in the Y-axis compression, yields the structure generally more pliant. This pattern resembles the observations made when comparing

lamellar structures in two perpendicular loading modes, although the difference is arguably (and expectedly) less pronounced.

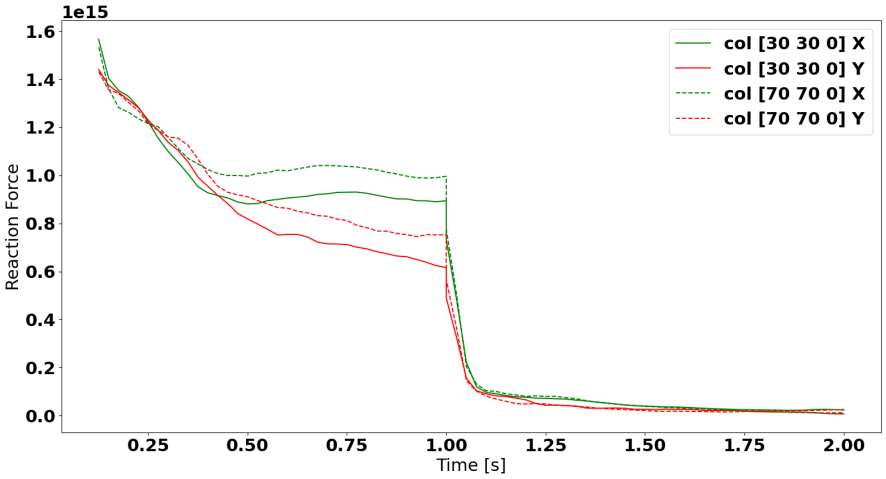

Figure 6.9: Comparison of X and Y axis compression results for two columnar structures.

6.2.3 Cubic structures

Similarly to the columnar structures, the analysis of the individual plots, graphed according to the previously selected θ identities, proved to be relatively challenging. Nevertheless, the visualisation of the plots of cubic structures where all three parameters θ were equal, displays a pattern in the stiffness responses. As displayed in figure 6.10, the resistance to compression is stronger in the topologies with lower θ values. Furthermore, a distinctive feature emerges in the response of the cubic structure, setting it apart from the other two topologies. Following an initial sharp stiffness decrease, the cubic structure's stiffness response shows a partial recovery, and for some lower-angle structures results even in the increased logged reaction force with time, which was not observed as clearly for the other structures. One possible explanation for this observed pattern could be the effect of the self-contact interactions.
It also has to be noted that, as in the case of the topologies analysed previously, two cubic structures were observed to exhibit 'an outlier behaviour', specifically of configurations [20 50 50] and [20 70 70].

6.2.4 Comparison between different topology types

Five different cases were studied, i.e. the compression of lamellar topology parallel and perpendicular to its lamellae, the compression of columnar structure with columns aligned horizontally and vertically relative to the loading axis, as well as the compression of the cubic structure in one loading direction. All these modalities have been subsequently plotted on the same graph space, in an attempt to compare topologies with the same angle

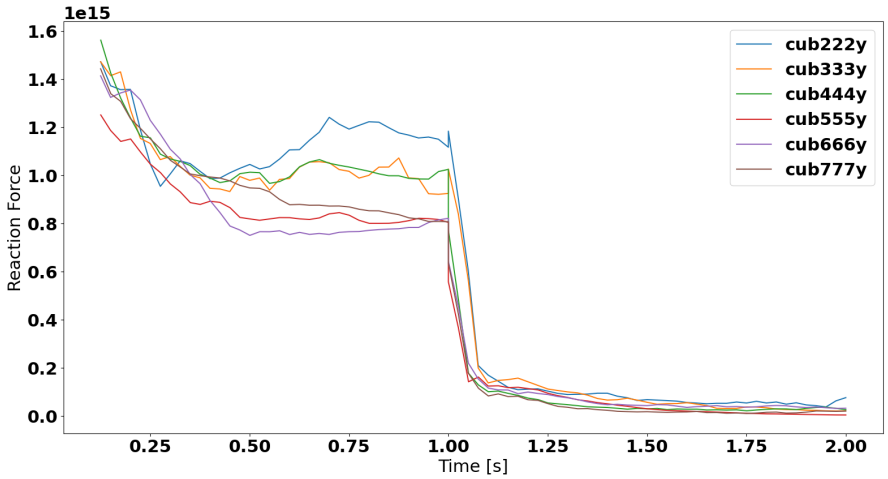

Figure 6.10: Comparison of cubic structures compressed in Y-axis for which θ_1=θ_2=θ_3.

values for the non-zero angles defining the structures. In terms of visual analysis, the plots seem to follow a general trend, visible for various angles considered. Figure **??**illustrates the reaction force of these five different test modalities relative to each other, for two set values of parameters θ. Both plots exhibit a similar pattern, which proved to be a recurring observation throughout the analysis of comparison graphs for various θ parameters. The lamellar structure compressed perpendicular to its lamellae showed the most resistance to compression; while the perpendicular loading of the lamellar structures resulted in the most compliant behaviour. Analogously, the vertical alignment of columns generally rendered the columnar structure stiffer in comparison to horizontal alignment, albeit with the difference being less pronounced between the two loading modes (as observed especially in the case of [40 40 0] structure). Compared to columnar topologies, cubic structures generally demonstrated similar or marginally higher stiffness response in the initial loading phase, and an overall greater resistance to compression as the loading progressed. However, cubic structures still generally showed more compliance relative to the lamellar topologies in X-axis compression. It is also worth mentioning that the highest value in terms of reaction force in an individual simulation was recorded for lamellar structure [0 20 0] compressed perpendicular to its lamellae.

6.3 Energy absorption

In the subsequent part of the analysis, the data was used to quantify the energy absorption for each structure. The energy for each simulation was computed using numpy.trapz command, which executed an integration along the time axis using the composite trapezoidal rule. For each type of structure, the energy was then plotted as a function of the respective theta angle. As it can be seen in figure 6.12, there is a clear distinction between the two modes of compression. Looking purely at the numerical values computed, the energy absorption for the compression occurring parallel to the lamellae (Y-axis) has,

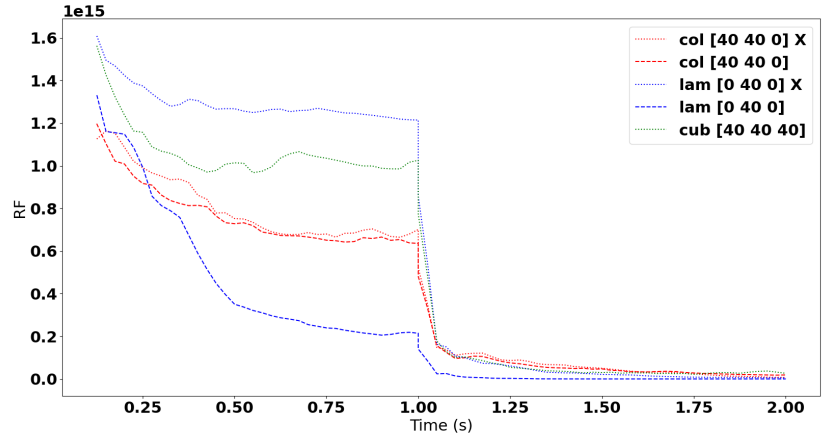

(a)

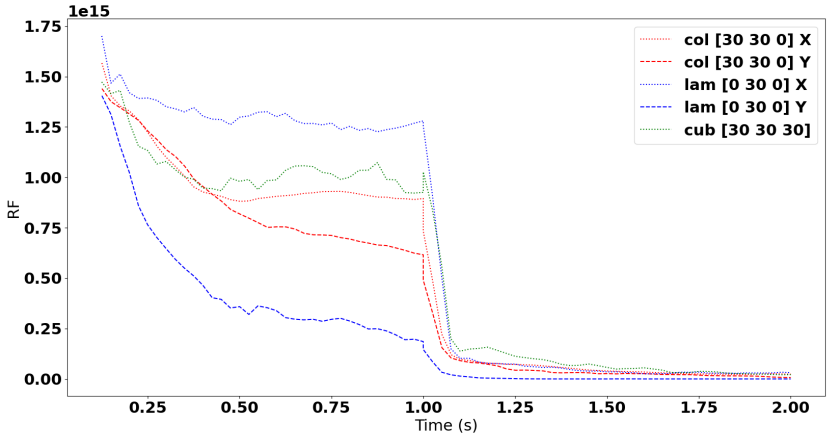

(b)

Figure 6.11: A comparison of columnar and lamellar structures compressed in the X-axis and Y-axis, and cubic structures compressed along the Y-axis for an arbitrary angle configuration, (a) 40 degrees and (b) 30 degrees.

on average, twice as large a value as the compression perpendicular to the lamellae. In the most extreme case, a structure with [0 20 0] theta angles exhibits almost a threefold increase in energy absorption between the two modalities. For columnar structures, since there were

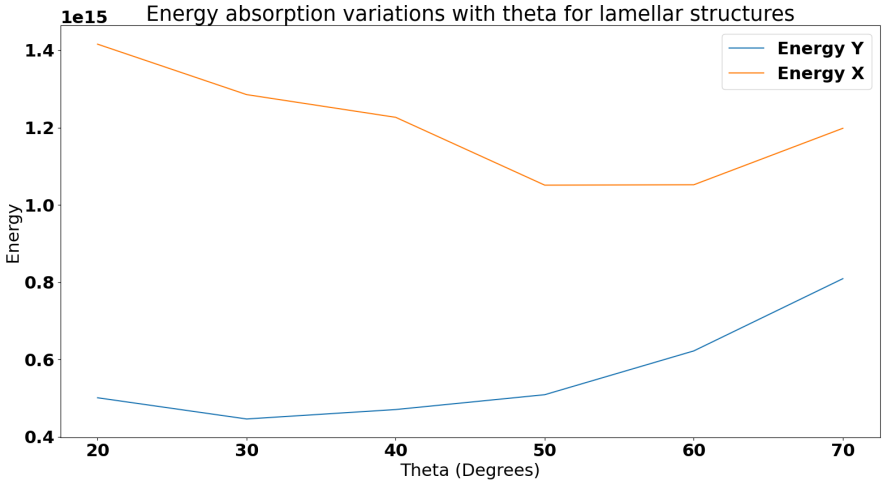

Figure 6.12: Variation of energy absorption with theta1 compression along the Y-axis and X-axis.

two parameters theta related to the output, i.e. the absorption energy, the data was compiled in a form of a histogram. As expected, there is a clear distinction between the

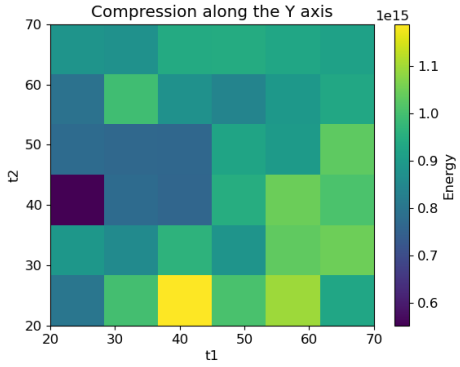

Figure 6.13: Variation of energy absorption with theta values for columnar structures. Compression along the Y-axis.

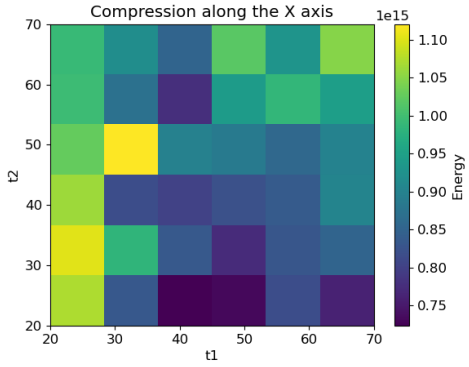

Figure 6.14: Variation of energy absorption with theta values for columnar structures. Compression along the X-axis.

patterns observed in the two heatmaps. Firstly, it can be observed that the difference in terms of the observed absolute energy values is not as large as in the lamellar structures. The results are also supporting the previous claim, that θ_1 is the parameter which has a stronger influence on the stiffness of columnar topologies compressed perpendicular to the alignment of columns, i.e. when columns are vertical with respect to the loading direction.

Analogously, the opposite is true for a horizontal column alignment. One can also notice that columnar [20 40 0] had significantly lower energy in the Y-axis compression. The result aligns with the earlier observation made during the visual analysis of the RF plots, wherein the reaction force recorded for this structure deviated significantly in comparison to other topologies.

6.3.1 Cubic structures

A similar plot was composed for cubic structures, as shown in Figure 6.15 The plot shows

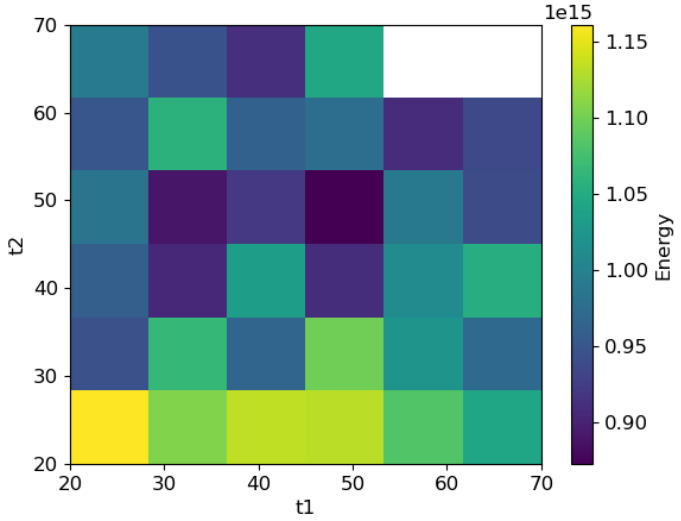

Figure 6.15: Variation of energy absorption with theta values for cubic structures.

that the compression energy is the highest for the structures with an angle configuration of [x 20 20]. Overall, one might make a hypothesis that θ_3 and $theta_2$ seem to have a larger impact on how much resistance the structure exhibits in response to the compression in this modality. It is also interesting to note that the lowest compression energy was observed for structures which have configurations close to [45 45 45].

6.4 Strain rate variations

In the subsequent part of the study, a brief analysis was conducted to explore the impact of strain rate variation on the mechanical behaviour of the selected spinodoid topologies. Due to the scope of the work and the time constraints, the decision was made to restrict this analysis to a single set of structures. The outcomes of this analysis were to be regarded as supplementary to the main study, with the aim to identify only the most general patterns; and which could also provide a basis for further studies in future work.
To aim for a more pronounced response, three spinodoid structures with small θ parameters were selected for analysis.

Lamellar [0 20 0], columnar [20 20 0] and cubic [20 20 20] topologies were selected for this test. Each of the structures was compressed in the Y-axis following the simulation settings described in the previous chapter, i.e. with a 1-second loading step and a 1-second holding step. After that, the loading step was increased to 2, and then to 3 seconds respectively. The reaction force was then plotted against time for each topology in all 3 strain rates, as presented in figure 6.16. The results indicate that the cubic structure shows the stiffest

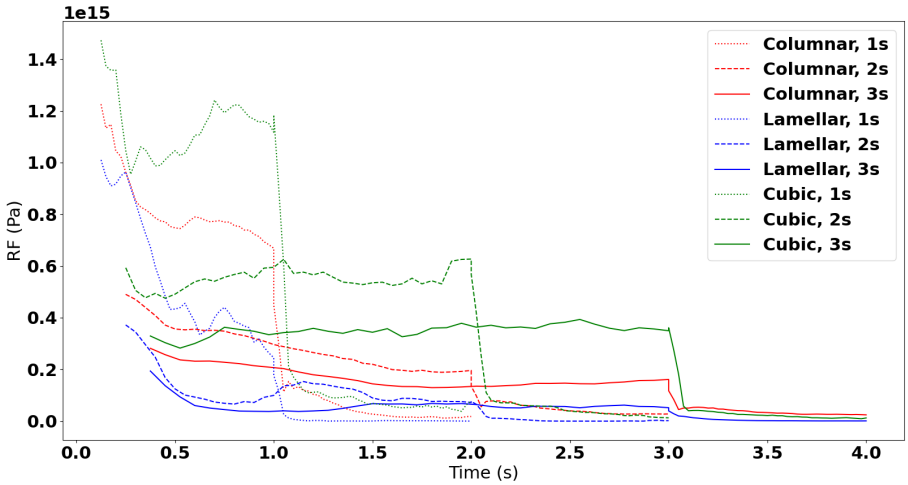

Figure 6.16: Strain rate variation for 1 to 3-second loading.

response in each of the three loading rates. For lamellar structures, the difference in the stiffness response for 2 and 3-second loading, especially after the initial 1-second, is almost identical. For cubic and columnar structures the difference is way more pronounced. Overall, the cubic structure was the stiffest in each of the three loading cases, while the lamellar structure was the most compliant. It is also interesting how for lamellar the initial plot shape changes so much with changing strain rate - very stiff initial response in 1 s loading, while for longer loading times the decrease in stiffness is more gradual.
Additionally, one can observe that the initial plot shape for the lamellar structure undergoes significant changes with varying strain rates. The topology exhibits an initial high resistance to deformation and a rapid decrease in stiffness in the 1-second loading condition; while for the two longer loading modes the decrease in stiffness is notably more gradual.

7 Machine learning model for mechanical response prediction

Based on the previously conducted analysis, the subsequent objective of the work was to train a simple machine learning model, which would generate the reaction force plots for the structures based on their θ parameters. The aim was to train an individual model for each of the topology classes, yielding three models in total. The purpose of building three distinct models was to simplify the data training process by pre-defining the topology class for each reaction force data which was used for training. Initially, the basis for the machine learning model was considered to be one of the two following approaches: Support Vector Regression (SVR) or Multi-output Decision Tree Regression. However, the SVR model allows for using only one input parameter; while for the desired model training multiple outputs were used. For this reason, Multi-output Decision Tree Regression was effectively selected. Python code was written to load the reaction force data into the system and to define input parameters. Libraries from *scikit-learn.org* were used for data splitting, model training and model evaluation.

7.1 Defining the model performance metrics

One of the most important parts of the machine learning model definition is its evaluation. there are multiple statistical tools available, and the choice of evaluation metric depends largely upon the type of the model application. In the initial attempt, R2 was quantified for both the test and training set. R-squared is a standard statistical metric used to evaluate machine learning models designed to solve problems associated with regression. It is calculated based on the following formula:

$$R^2 = 1 - \frac{SS_{res}}{SS_{tot}} \tag{7.1}$$

Where SS_{res} denotes the residual sum of squares of Y values predicted through regression; while SS_{tot} refers to the sum of squares of the average value for the variable Y, It is important to note that if the computed R-squared value shows a much better fit for the training set compared to the test set, it is a strong indication that the model is overfitting. As a result, the model becomes unable to generalize and predicts results aligned with the training set too closely. For this specific problem, since the data set especially for the lamellar structures is very small, the R-squared value was deemed unsuitable for evaluation. Therefore, to bypass that limitation, an approach using LeaveOneOut cross-validation with an Absolute Percentage Error (MAPE) as a performance metric. LeavOneOut is a subtype of K-fold cross-validation for which the test size is set to 1. MAPE is a conventional way of measuring the

accuracy of the models for which the data size is small, and it can be calculated using the following formula:

$$\text{MAPE} = \frac{1}{n}\sum_{t-1}^{n}\left|\frac{A_t - F_t}{A_t}\right| \tag{7.2}$$

where A_t stands for the actual Y-value and F_t, refers to the value obtained due to forecasting, i.e. the outcome of the model prediction.

7.2 Results of ML model predictions

7.2.1 Computing the evaluation metrics

Ultimately, for each spinodoid topology type, a separate model was built. Only the compression along the Y-axis was considered in the analysis. Subsequently, MAPE was calculated to evaluate all possible test/training splits, yielding 6 results for lamellar structures,36 for columnar topologies, and 34 for cubic. The computed MAPE values were then compared to observe how its variations with different splits.
For cubic structures, the average MAPE was calculated to be 0.4021. For columnar structures in Y-axis compression, the MAPE value averaged 0.641134467. It has to be noted, however, that for 3 structures in particular the MAPE values were significantly higher than for the other splits. Particularly for the split with columnar configuration [30 40 0], the calculated MAPE is above 7; while for all other splits except two, MAPE values do not exceed unity. However, when the 3 data points with the highest MAPE were removed, the average value for the metric dropped to 0.374597989. For the lamellar dataset, MAPE proved to be an unreliable metric, as for two out of six splits the metric was calculated to be of the order of 10e27. This is presumably due to a very small sample size, i.e. 6 splits only, or due to a possible numerical instability caused by the high order of magnitude of the reaction force itself.

7.2.2 Visualisation of the predicted reaction force graphs

As described in the previous section, a code was written to train a simple machine model to try to predict the force distribution in time based on a theta value assigned to the model. The script was then extended to include also the visualisation of the predicted plots for an arbitrary split. Figure 7.1 shows the first obtained plot, a prediction for a lamellar structure. The same algorithm was used to predict an arbitrary RF plot in time for cubic structures. Figure 7.2 shows one of the approximations. However, as can be observed from the visual inspection, MAPE does not provide the best metric for prediction accuracy. Figure 7.3 shows a predicted curve for another split, which has an equal value of calculated MAPE as figure 7.2, yet as visible on the plot, displays significantly worse fitting. Very similar results were observed for columnar structures.

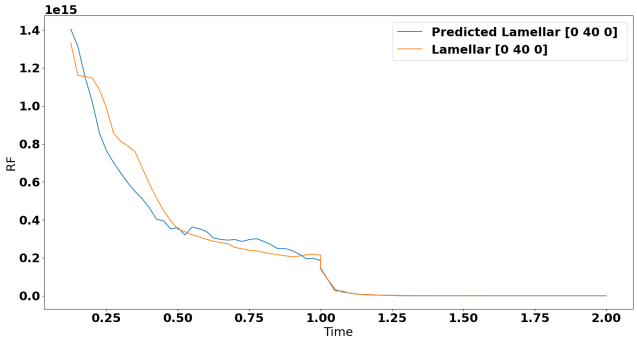

Figure 7.1: An example for model prediction, trained on 5 simulated lamellar models and tested on lamellar [0 40 0]

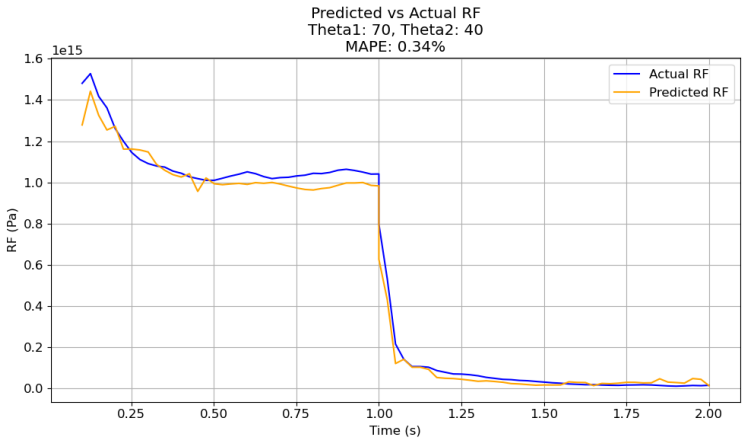

Figure 7.2: An example of model prediction, trained on 34 simulated cubic models.

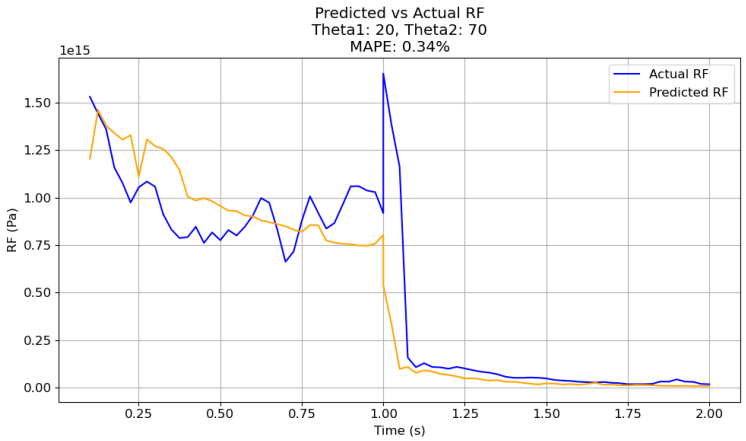

Figure 7.3: An example for poor model prediction, trained on 34 simulated cubic models.

8 Conclusions and future research directions

8.1 Simulation design consideration

Overall, the design of an appropriate FEM model is often linked to many challenges. The critical assessment of the FEM analysis results is therefore a crucial step. While selecting values for model generation, a balance needed to be struck. Increasing parameters such as the topology resolution and the number of elements contained within the mesh lead to extended simulation times. Similarly, the computation time increases with a higher frame log setting. Therefore, in an effort to optimize the process, intermediate values were selected for each of these parameters. Similarly, as described earlier, a mass scaling factor was introduced as a compromise in the simulation to improve computing efficiency. In future studies, it would be very beneficial to attempt to remove the mass scaling for improved accuracy of the model. It would be also very beneficial to perform a resolution convergence study in a way that it was done for the wave number convergence; however, due to the random seed used in the periodic spinodoid code which was studied initially, generating structures with a set wave number but different resolutions yielded different topologies, i.e. each time a resolution was tailored a new topology would be generated. Hence, the resolution was chosen based on an assumption. Due to the time constraints of the work, the resolution convergence study was not repeated for the non-periodic structures which ended up being the main focus of the report, and which do not show the same pattern in terms of inconsistent topology generation for varied resolution. It is speculated that a significant improvement could have been achieved had the model been defined in terms of the implicit solver rather than the explicit solver. Furthermore, the decision related to the time step and time interval definition has important implications for the solver used. For a more detailed strain rate analysis, further study could involve careful consideration of discretization and time step choice. An increased number of frames, which is expensive in terms of processing times, could potentially significantly improve the accuracy of the model.

8.1.1 Material selection evaluation

The next step in the simulation evaluation is the consideration of the material selection, as well as a choice of the underlying constitutive model. Due to the scope and time constraints of this work, only one constitutive model was considered. It has to be acknowledged, however, that the Maxwell model is the most simplified depiction of viscoelasticity, and for many viscoelastic materials studied it might not provide an accurate representation of their behaviour. In the continuation of this work, exploring the Burgers model, Kelvin-Voigt model, or a combination of all three, and subsequently comparing

their effectiveness would be very beneficial. Eventually, more complex viscoelastic models could also be implemented. The exploration of non-linear viscoelasticity, volume changes in the material, or the introduction of anisotropy in terms of regime definition, e.g. transversely isotropic viscoelasticity could also be included in future work. All the structures generated were of the same density. Future works could potentially focus on the impact of density on the mechanical behaviour of spinodoids. It would be particularly interesting to investigate the effect of tailoring the density with respect to specific bone properties, particularly the porosity of the trabecular bone.
One of the most interesting aspects of future studies, particularly in terms of bone biomaterials, would involve the study of bone remodelling. The introduction of the adaptive mechanical properties in the simulation is, however, a challenging problem, and significant consideration should be made before implementing it. Nevertheless, the context of bone biomaterials has been used merely as an example of a potential application. In principle, polymer-based spinodoid structures could potentially find application in a range of different fields. One possible direction involves energy absorption items like bike helmets, or such as running shoe soles. Hence, examining their behaviour in response to this loading and exploring the design space holds significant utility for a more universal context. Therefore, in hindsight, a significant improvement of the project would be to put less emphasis on fine-tuning simulation parameters and instead adopt a broader scope. Becoming too fixated on a singular application of the studied concept, even if it provides a convincing starting point for the analysis, could inadvertently negatively affect productivity and limit the overall perspective of the research.

8.2 The evaluation of the simulation results

Overall, the analysis of the simulation results brought several interesting insights. Firstly, a clear distinction was observed when comparing the compression of lamellar and columnar structures in two modalities. The obtained results were in agreement with the predefined assumptions, i.e. the compression parallel to lamellae and horizontal columns would yield the spinodoid more compliant. The evident emergence of patterns showcasing the highest absorption energy depicted in the histograms (and plots for the lamellar structures) was also notable. Remarkably, against the expectations cubic structures were discovered to exhibit the highest resistance to deformation, surpassing the columnar structures with vertically aligned columns. It would be interesting to repeat the simulation for larger compressions and/or varied compression rates and see if the pattern persists. Additionally, investigating whether similar trends persist under conditions where the sampling of theta angles is randomized could be worthwhile. Another point worth considering is the presence of the outlier spinodoids, and consequently, the measures one can take in order to prevent their impact on simulation data. While one viable solution involves their exclusion from the analysis, this approach is ethically questionable, and not sustainable in the long term analysis. Based on the experience from this work, remeshing the structures and subsequently re-running the simulations can solve the issue for individual structures, albeit at the expense of considerable computational resources and time, as the procedure itself is generally rather exhaustive.
Hence revolves around automating the meshing procedure. Developing a script to automate meshing within hypermesh, coupled with intermediate steps for continuous mesh assessment, could significantly accelerate any future simulations. Additionally, the requirements for the mesh quality could be redefined in order to ensure that the

appropriate mesh quality is met for each individual topology.
For the vast majority of the simulations, the reaction force during the holding step dropped to zero almost instantaneously, occasionally resulting in a sharp spike in reaction force at the step transition. One potential explanation for that observation is the relatively small compression of the structure. It can be speculated that if a larger displacement was applied on the top plane, a more pronounced effect of stress relaxation could be observed. Moreover, as suggested previously, a more in-depth study of strain rate impact would be very beneficial. In this study, some variation in terms of the transition from the loading step to the holding step was already observed, i.e. a mild stress relaxation effect was observed for shorter loading times tested, hence it would be interesting to try loading simulation for shorted times to try observing more accentuated stress relaxation. It would be also interesting to explore the changes in the stress relaxation patterns through variations in the holding step definition. For example, one could introduce a more gradual transition to a holding step by creating an intermediate step with a slower loading rate, or carefully tuned loading amplitude. This could also help with minimizing the effect of sharp spikes upon step transition visible for some structures. However, it seems plausible that the occurrence of this spike is rather due to either the errors in the meshing or due to errors in the interaction/contact definition. This is concluded based on the fact that if the spike was observed in a structure, it was present in both the X-axis and the Y-axis loading. Therefore, in general, the presence of the spike on its own was not assigned any significance in terms of the mechanical behaviour analysis and was rather treated as noise/random simulation artefact, similar to the initial spike in reaction force upon surface contact establishment, observed for first 2-3 points registered for compression of each topology.

8.3 Machine learning model predictions

Overall, the predictions generated through the model were rather satisfactory for columnar and cubic topologies, except for very few outlier structures. A potential improvement to this analysis could involve testing different regression algorithms or including additional pre-processing strategies before training the model. Alternatively, an algorithm could be implemented to exclude the outlier structures from the analysis. Finally, increasing the size of the training set could significantly improve the quality of prediction, however, this is intrinsically linked with a significant increase in the data generation times.

8.4 Other future analysis directions

Regarding other potential future directions, further studies could involve tackling the inverse property-structure design as described in the paper by Kumar et al. [5], especially in a viscoelastic regime. A very interesting study direction would involve the attempt to tailor the anisotropy to specific bone properties, based on real-life data. A promising avenue of research lies also in the exploration of biocompatibility enhancements, and relating the topology generation to factors such as porosity and pore anisotropy, or the impact of curvature.

Bibliography

[1] L.M.R.Machado J.V.L.daSilva B.M.Manzini P.Y.Noritomi. "Advances in Bone tissue engineering: A fundamental review". In: *Journal of Biosciences* 46.1 (2021), pp. 1–18.

[2] Fengqing Shang et al. "Advancing application of mesenchymal stem cell-based bone tissue regeneration". In: *Bioactive materials* 6.3 (2021), pp. 666–683.

[3] Youwen Yang et al. "Mg bone implant: Features, developments and perspectives". In: *Materials & Design* 185 (), p. 108259.

[4] PV Evdokimov et al. "Adaptable metamaterials based on biodegradable composites for bone tissue regeneration". In: *Inorganic Materials: Applied Research* 12.2 (2021), pp. 404–415.

[5] Siddhant Kumar et al. "Inverse-designed spinodoid metamaterials". In: *npj Computational Materials* 6.1 (2020), pp. 1–10.

[6] Zhifei Dong and Xin Zhao. "Application of TPMS structure in bone regeneration". In: *Engineered Regeneration* 2 (2021), pp. 154–162.

[7] Elaine Nicpon Marieb and Katja Hoehn. *Human anatomy & physiology*. Pearson education, 2007.

[8] Chrysoula Chatzigeorgiou et al. "Numerical investigation of the effective mechanical properties and local stress distributions of TPMS-based and strut-based lattices for biomedical applications". In: *Journal of the mechanical behavior of biomedical materials* 126 (2022), p. 105025.

[9] David F Williams. "On the nature of biomaterials". In: *Biomaterials* 30.30 (2009), pp. 5897–5909.

[10] David F Williams. "On the mechanisms of biocompatibility". In: *Biomaterials* 29.20 (2008), pp. 2941–2953.

[11] Amir A Zadpoor. "Mechanical performance of additively manufactured meta-biomaterials". In: *Acta biomaterialia* 85 (2019), pp. 41–59.

[12] Meng-Ting Hsieh, Matthew R Begley, and Lorenzo Valdevit. "Architected implant designs for long bones: Advantages of minimal surface-based topologies". In: *Materials & Design* 207 (2021), p. 109838.

[13] Elvan Dogan et al. "3D Printing metamaterials towards tissue engineering". In: *Applied materials today* 20 (2020), p. 100752.

[14] HMA Kolken. "Poisson meets Escher. Exploring the Poisson effect in bone implant design". In: (2022).

[15] Xiaoyu Zheng et al. "Ultralight, ultrastiff mechanical metamaterials". In: *Science* 344.6190 (2014), pp. 1373–1377.

[16] HMA Kolken et al. "Additively manufactured space-filling meta-implants". In: *Acta Biomaterialia* 125 (2021), pp. 345–357.

[17] Michael A Webb et al. "Chemically specific dynamic bond percolation model for ion transport in polymer electrolytes". In: *Macromolecules* 48.19 (2015), pp. 7346–7358.

[18] Meng-Ting Hsieh et al. "The mechanical response of cellular materials with spinodal topologies". In: *Journal of the Mechanics and Physics of Solids* 125 (2019), pp. 401–419.

[19] EP Favvas and A Ch Mitropoulos. "What is spinodal decomposition". In: *J. Eng. Sci. Technol. Rev* 1.1 (2008), pp. 25–27.

[20] Björn König, Olivier JJ Ronsin, and Jens Harting. "Two-dimensional Cahn–Hilliard simulations for coarsening kinetics of spinodal decomposition in binary mixtures". In: *Physical Chemistry Chemical Physics* 23.43 (2021), pp. 24823–24833.

[21] Celal Soyarslan et al. "3D stochastic bicontinuous microstructures: Generation, topology and elasticity". In: *Acta materialia* 149 (2018), pp. 326–340.

[22] Jan-Hendrik Bastek et al. "Inverting the structure–property map of truss metamaterials by deep learning". In: *Proceedings of the National Academy of Sciences* 119.1 (2022).

[23] Li Zheng, Siddhant Kumar, and Dennis M Kochmann. "Data-driven topology optimization of spinodoid metamaterials with seamlessly tunable anisotropy". In: *Computer Methods in Applied Mechanics and Engineering* 383 (2021), p. 113894.

[24] Anna Guell Izard et al. "Ultrahigh energy absorption multifunctional spinodal nanoarchitectures". In: *Small* 15.45 (2019), p. 1903834.

[25] Carlos M Portela et al. "Extreme mechanical resilience of self-assembled nanolabyrinthine materials". In: *Proceedings of the National Academy of Sciences* 117.11 (2020), pp. 5686–5693.

[26] Sebastien JP Callens et al. "The local and global geometry of trabecular bone". In: *Acta Biomaterialia* 130 (2021), pp. 343–361.

[27] AV Okulov et al. "Dealloying-based metal-polymer composites for biomedical applications". In: *Scripta Materialia* 146 (2018), pp. 290–294.

[28] Shenlong Wang, Yajie Xu, and Jiacheng Li. "Stationary probability densities of generalized Maxwell-type viscoelastic systems under combined harmonic and Gaussian white noise excitations". In: *Journal of the Brazilian Society of Mechanical Sciences and Engineering* 42 (2020), pp. 1–9.

[29] Montgomery T Shaw and William J MacKnight. *Introduction to polymer viscoelasticity*. John Wiley & Sons, 2018.

[30] L Wang. *Chapter 6—one-dimensional visco-elastic waves and elastic-visco-plastic waves Foundations of Stress Waves ed L Wang*. 2007.

[31] D Yogi Goswami. *The CRC handbook of mechanical engineering*. CRC press, 2004.

[32] Patrick Brewick, Robert Saunders, and Amit Bagchi. *Biomechanical modeling of the human head*. Tech. rep. NAVAL RESEARCH LAB WASHINGTON DC WASHINGTON United States, 2017.